A hybrid recursive regularized lattice Boltzmann model with overset grids for rotating geometries

H. Yoo, M. Bahlali, Julien Favier, Pierre Sagaut

H. Yoo, M. Bahlali, Julien Favier, Pierre Sagaut. A hybrid recursive regularized lattice Boltzmann model with overset grids for rotating geometries. Physics of Fluids, 2021, 33 (5), pp.057113. 10.1063/5.0045524 . hal-03597721

HAL Id: hal-03597721
https://hal.science/hal-03597721v1

A hybrid recursive regularized lattice Boltzmann model with overset grids for rotating geometries

H. Yoo (유희식),[a] **M. L. Bahlali,** **J. Favier,** **and P. Sagaut**

AFFILIATIONS

Aix Marseille University, CNRS, Centrale Marseille, M2P2 UMR 7340, Marseille, France

ABSTRACT

Simulating rotating geometries in fluid flows for industrial applications remains a challenging task for general fluid solvers and in particular for the lattice Boltzmann method (LBM) due to inherent stability and accuracy problems. This work proposes an original method based on the widely used overset grids (or Chimera grids) while being integrated with a recent and optimized LBM collision operator, the hybrid recursive regularized model (HRR). The overset grids are used to actualize the rotating geometries where both the rotating and fixed meshes exist simultaneously. In the rotating mesh, the fictitious forces generated from its non-inertial rotating reference frame are taken into account by using a second order discrete forcing term. The fixed and rotating grids communicate with each other through the interpolation of the macroscopic variables. Meanwhile, the HRR collision model is selected to enhance the stability and accuracy properties of the LBM simulations by filtering out redundant higher order non-equilibrium tensors. The robustness of the overset HRR algorithm is assessed on different configurations, undergoing mid-to-high Reynolds number flows, and the method successfully demonstrates its robustness while exhibiting the second order accuracy.

I. INTRODUCTION

The lattice Boltzmann method (LBM) has attracted huge attention from the computational fluid dynamics community over the last few decades for its efficiency and its relatively easy numerical implementation on Cartesian meshes avoiding the use of body-fitted grids. However, stability still remains a crucial issue for high Reynolds number and compressible flows. In that context, the regularized method was suggested to improve the stability properties of the LBM collision operator.[1] The method regularizes the non-equilibrium functions at the pre-collision steps, by excluding redundant high order non-equilibrium parts which would not be necessary to recover the Navier–Stokes equation. It is conducted by reconstructing the low order non-equilibrium parts from the low order macroscopic non-equilibrium tensors, computed by projecting the non-equilibrium parts into the low order Hermite polynomials. Subsequently, the recursive regularization method was suggested to increase the orders of the regularized non-equilibrium tensors by using the recursive formula.[2,3] The recursive regularization showed an improvement of the stability of the overall algorithm compared to the standard single-relaxation time model (SRT) and multi-relaxation time model (MRT) at moderate to high Reynolds numbers. More recently, the hybrid recursive regularized model (HRR) was proposed[4] based on the reconstruction of the non-equilibrium tensors by the non-equilibrium distribution functions but also by macroscopic stress tensors calculated from finite difference schemes. The part of the non-equilibrium tensors computed with the finite difference schemes results in injecting a hyperviscosity in the flows, which increases the stability of the solver. The HRR collision model has thus been actively studied and applied to various challenging configurations, compressible flows for instance.[5,6] Also, its capability to overcome the spurious numerical effects induced by the interfaces of mesh refinement was demonstrated.[7] Extensive studies based on linear stability analysis also showed that the HRR model can suppress the non-physical spurious modes and improve the stability of the global scheme.[8,9]

Simulating accurately rotating objects immersed in fluid flows is a major issue for industrial applications. For rigid rotating bodies at moderate Reynolds and Mach number flows, different solutions such as the immersed boundary method[10–15] and the overset local reference frame (LRF) method[16–20] were proposed. The immersed boundary method is an efficient way to simulate moving and deformable geometries, but suffers from a low-order of accuracy, which could be an issue in the case of turbulent high Mach number flows. The overset local reference frame method (overset LRF), also referred to as Chimera mesh or sliding mesh, is widely and successfully applied for industrial applications due to the possibility of using refined grids to resolve near-wall turbulent eddies. However, in the context of the LBM, this class of methods is facing stability issues when the local Mach number reaches high values in the vicinity of the rotating region.[16,17,19,20]

In principle, the overset method is based on two different meshes simultaneously, which raises important issues on how to compute the fictitious forces generated by the rotating non-inertial frame and how to interpolate quantities between meshes. In the LBM, several overset approaches have been tested in the literature. Among them, a standard Bhatnagar–Gross–Krook (BGK) collision model combined with overset sliding meshes and a second order discrete forcing term has been proposed.[16,17] A cumulant lattice Boltzmann method has also been proposed with overset sliding meshes,[19] which showed a second order accuracy at low Mach and low Reynolds number flows. Also, an implementation using the multi-relaxation time collision model has been proposed to study the noise generated by rotating walls.[20]

Based on these works, and within the scope of simulating rotating geometries in industrial flows, we propose here to integrate the overset method with the HRR collision model. To the best of the authors' knowledge, this is the first time that the overset method is tested with the regularization based collision model. The method is validated through its second order accuracy at different configurations, and also, its aerodynamic properties are well matched with the references. The proposed algorithm is assessed in mid-to-high Reynolds number flows, keeping the non-dimensional relaxation times between 0.5 and 0.6. The paper is organized as follows: the HRR collision model and the proposed overset method are presented in Sec. II and Sec. III; the accuracy of the overall algorithm is then studied in Sec. IV, before validating the model in Sec. V on various test cases; and the conclusions are in Sec. VI.

II. THE HYBRID RECURSIVE REGULARIZED LATTICE BOLTZMANN METHOD

Originating from the discretization of the Boltzmann equation, the lattice Boltzmann method (LBM) describes the motion of fluids through the collision and streaming of fluid particles, described by their distribution functions, which relate to the probability of having a fluid particle at a given velocity, at a given position in space, and at a given instant.

The lattice refers to the space discretization, which is classically a simple Cartesian mesh in the LBM. At each lattice point, a set of discrete particle velocities are defined, allowing the fluid particles to head toward a finite set of directions, chosen as a function of the accuracy and physical contents of the LBM model. By discretizing the Boltzmann equation in space, time, and particle velocity, a transport equation for the distribution functions is obtained,

$$f_i(\boldsymbol{x}+\boldsymbol{c}_i\Delta t, t+\Delta t) - f_i(\boldsymbol{x}, t) = -\frac{\Delta t}{\tau} f_i^{neq}, \tag{1}$$

where the index i refers to the discretization in the space of fluid velocities, $\boldsymbol{c}_i$ refers to the discrete velocities, and f_i^{neq} refers to the non-equilibrium part of the distribution function $f_i(\boldsymbol{x}, t)$, given by $f_i^{neq} = f_i(\boldsymbol{x}, t) - f_i^{eq}$, with f_i^{eq} the equilibrium part of the distribution functions, which will be detailed hereafter. The classical normalization $\Delta x = \Delta t = 1$ will be used hereafter, where Δx denotes the mesh size.

The left hand side of (1) represents the streaming process and its right hand side represents the simplest and widely used collision model, referred to as the Bhatnagar–Gross–Krook operator (BGK).[21] For more details, the reader is referred to Ref. 22. At each instant, the macroscopic characteristics for the fluids such as velocity, density, and stresses are easily reconstructed by taking the moments of the distribution functions. For instance, the fluid density is the moment of order 0, the fluid momentum is the moment of order 1 of the distribution function, and the stress tensor is obtained by taking the moment of order 2 of the non-equilibrium part of the distribution function.

By applying the Chapman–Enskog expansion,[23] the distribution function can be expanded with respect to the Knudsen number ε,

$$f_i = f_i^{eq} + \varepsilon f_i^{(1)} + \varepsilon^2 f_i^{(2)} + \cdots. \tag{2}$$

The zeroth order corresponds to the equilibrium function, and the rest of higher order terms are expansion of the non-equilibrium functions according to different Knudsen numbers.

The regularized method enhances the stability and accuracy of the collision and streaming processes by truncating redundant higher order non-equilibrium terms.[1–3] It aims at keeping the low order of the non-equilibrium terms which are sufficient to recover the macroscopic shear stress, while filtering out all the rest of higher order terms which are not essential. The original regularization method drops out all the non-equilibrium terms except for the second order non-equilibrium part, by projecting the non-equilibrium term to the second order Hermite polynomial $\mathscr{H}_i^{(2)}$.[1] It is based on the assumption that the second order non-equilibrium term could represent all the non-equilibrium parts $[\varepsilon f_i^{(1)} \simeq (f_i - f_i^{eq})]$. This second order non-equilibrium part can be reconstructed from the second order non-equilibrium tensor [from now on, all f_i's stand for the values including the Knudsen number ε in Eq. (2)],

$$a_{1,\alpha\beta}^{(2)} = \Sigma_i \mathscr{H}_i^{(2)}(f_i - f_i^{eq}) = \Sigma_i (c_{i\alpha}c_{i\beta} - \delta_{\alpha\beta}c_s^2)(f_i - f_i^{eq}). \tag{3}$$

However, the recursive regularization method (RR) allows us to keep the few more finite numbers of low order non-equilibrium tensors.[2,3] Using the recursivity formula of the Hermite polynomials, the method is able to hold finite orders of non-equilibrium tensors $\boldsymbol{a}_1^{(n)}$. As it provides freedom to expand the orders of the non-equilibrium tensors to be retained, it contributes to improving the stability. The third order non-equilibrium tensors are added based on the recursive formula,

$$a_{1,\alpha\alpha\beta}^{(3)} = 2u_\alpha a_{1,\alpha\beta}^{(2)} + u_\beta a_{1,\alpha\alpha}^{(2)}, \tag{4}$$

where isotropic tensors such as $a_{1,xxx}^{(3)}$ have to be excluded in the D3Q19 lattice.

These methods were further improved introducing the hybrid recursive regularized method (HRR),[4] in which two different ways to construct the second order non-equilibrium tensor $\boldsymbol{a}_1^{(2)}$ are hybridized. The first one is the second order non-equilibrium tensor as in the normal recursive regularization method [see Eq. (3)]. The second one relies on the shear stress $\boldsymbol{S}^{FD}$ calculated using a second-order accurate centered finite difference scheme,

$$a_{1,\alpha\beta}^{(2),FD} = -2\rho\tau c_s^2 \boldsymbol{S}^{FD}, \tag{5}$$

$$\boldsymbol{S}^{FD} = (\partial_\beta u_\alpha + \partial_\alpha u_\beta)/2. \tag{6}$$

The second order non-equilibrium tensor of the HRR method $\boldsymbol{a}_1^{(2),HRR}$ is defined as a linear combination of the non-equilibrium tensor computed by the second order moment of non-equilibrium distribution function $\boldsymbol{a}_1^{(2)}$ and the non-equilibrium tensor computed from finite difference $\boldsymbol{a}_1^{(2),FD}$,

$$a_{1,\alpha\beta}^{(2),HRR} = \sigma a_{1,\alpha\beta}^{(2)} + (1-\sigma) a_{1,\alpha\beta}^{(2),FD}. \tag{7}$$

This additive finite difference part works as injecting artificial viscosity in flow fields, which improves the numerical stability.[4,7–9]

Then, the third order non-equilibrium tensors of the HRR model $\boldsymbol{a}_1^{(3),HRR}$ are computed from the given second order non-equilibrium tensors [Eq. (7)] and the recursive formula [Eq. (4)], which is exactly the same procedure as the normal recursive regularization method.

Finally, the non-equilibrium parts of the HRR model could be reconstructed by projecting the different orders of the non-equilibrium tensors to the Hermite polynomials $\mathscr{H}_i^{(n)}$,

$$\begin{aligned}
f_i^{(1)} = w_i \Bigg(& \frac{1}{2c_s^4}\mathscr{H}_i^{(2)} : \boldsymbol{a}_1^{(2)} \\
& + \frac{1}{2c_s^6}(\mathscr{H}_{i,xxy}^{(3)} + \mathscr{H}_{i,yzz}^{(3)})(a_{1,xxy}^{(3)} + a_{1,yzz}^{(3)}) \\
& + \frac{1}{2c_s^6}(\mathscr{H}_{i,xzz}^{(3)} + \mathscr{H}_{i,xyy}^{(3)})(a_{1,xzz}^{(3)} + a_{1,xyy}^{(3)}) \\
& + \frac{1}{2c_s^6}(\mathscr{H}_{i,yyz}^{(3)} + \mathscr{H}_{i,xxz}^{(3)})(a_{1,yyz}^{(3)} + a_{1,xxz}^{(3)}) \\
& + \frac{1}{6c_s^6}(\mathscr{H}_{i,xxy}^{(3)} - \mathscr{H}_{i,yzz}^{(3)})(a_{1,xxy}^{(3)} - a_{1,yzz}^{(3)}) \\
& + \frac{1}{6c_s^6}(\mathscr{H}_{i,xzz}^{(3)} - \mathscr{H}_{i,xyy}^{(3)})(a_{1,xzz}^{(3)} - a_{1,xyy}^{(3)}) \\
& + \frac{1}{6c_s^6}(\mathscr{H}_{i,yyz}^{(3)} - \mathscr{H}_{i,xxz}^{(3)})(a_{1,yyz}^{(3)} - a_{1,xxz}^{(3)}) \Bigg),
\end{aligned} \tag{8}$$

where w_i and c_s are, respectively, the lattice weights and the speed of sound, and the second and third order Hermite polynomials read

$$\begin{aligned}
\mathscr{H}_{i,\alpha\beta}^{(2)} &= c_{i\alpha}c_{i\beta} - \delta_{\alpha\beta}c_s^2, \\
\mathscr{H}_{i,\alpha\beta\gamma}^{(3)} &= c_{i\alpha}c_{i\beta}c_{i\gamma} - c_{i\gamma}\delta_{\alpha\beta}c_s^2 - c_{i\beta}\delta_{\gamma\alpha}c_s^2 - c_{i\alpha}\delta_{\beta\gamma}c_s^2.
\end{aligned} \tag{9}$$

Also, the third order equilibrium function is employed as[4,6]

$$\begin{aligned}
f_i^{eq} = w_i \Bigg(& \rho + \rho\frac{\boldsymbol{c}_i \cdot \boldsymbol{u}}{c_s^2} + \frac{\rho}{2c_s^4}((\boldsymbol{c}_i \cdot \boldsymbol{u})^2 - c_s^2\boldsymbol{u}^2) \\
& + \frac{1}{2c_s^6}(\mathscr{H}_{i,xxy}^{(3)} + \mathscr{H}_{i,yzz}^{(3)})(a_{0,xxy}^{(3)} + a_{0,yzz}^{(3)}) \\
& + \frac{1}{2c_s^6}(\mathscr{H}_{i,xzz}^{(3)} + \mathscr{H}_{i,xyy}^{(3)})(a_{0,xzz}^{(3)} + a_{0,xyy}^{(3)}) \\
& + \frac{1}{2c_s^6}(\mathscr{H}_{i,yyz}^{(3)} + \mathscr{H}_{i,xxz}^{(3)})(a_{0,yyz}^{(3)} + a_{0,xxz}^{(3)}) \\
& + \frac{1}{6c_s^6}(\mathscr{H}_{i,xxy}^{(3)} - \mathscr{H}_{i,yzz}^{(3)})(a_{0,xxy}^{(3)} - a_{0,yzz}^{(3)}) \\
& + \frac{1}{6c_s^6}(\mathscr{H}_{i,xzz}^{(3)} - \mathscr{H}_{i,xyy}^{(3)})(a_{0,xzz}^{(3)} - a_{0,xyy}^{(3)}) \\
& + \frac{1}{6c_s^6}(\mathscr{H}_{i,yyz}^{(3)} - \mathscr{H}_{i,xxz}^{(3)})(a_{0,yyz}^{(3)} - a_{0,xxz}^{(3)}) \Bigg),
\end{aligned} \tag{10}$$

where the third equilibrium tensors are $a_{0,\alpha\beta\gamma}^{(3)} = \rho u_\alpha u_\beta u_\gamma$ and $\boldsymbol{u}^2$ is the vector norm.

Eventually, from the given equilibrium and regularized non-equilibrium functions, the HRR collision operator in the inertial fixed frame is defined as

$$f_i(\boldsymbol{x} + \boldsymbol{c}_i\Delta t, t + \Delta t) = f_i^*(\boldsymbol{x}, t) = f_i^{eq}(\boldsymbol{x}, t) + \left(1 - \frac{\Delta t}{\tau}\right) f_i^{(1)}(\boldsymbol{x}, t). \tag{11}$$

Note that the Galilean invariance is not corrected explicitly, which corresponds to an $O(u^3)$ error added on the non-equilibrium tensor, following the standard HRR method.[2–4,7]

III. OVERSET LOCAL REFERENCE FRAME METHOD (LRF)

In the overset local reference frame (LRF) approach, two different meshes exist at the same time, with different reference frames. The background fixed mesh has an inertial/Galilean reference frame, whereas the rotating mesh has a non-inertial/non-Galilean reference frame. Therefore, in the rotating region, this non-inertial reference frame requires using the fictitious forces at each time step. The communications between moving and fixed grids involve the interpolations of macroscopic values, modifying them to take into account the geometrical and inertial features of the newly interpolated region and reconstructing the distribution functions from the interpolated macroscopic values. In this section, we detail the different steps of the communications between grids.

A. The discrete forcing scheme in the HRR model

In the non-inertial rotating frame, the fictitious forces such as the Coriolis and centrifugal forces have to be considered as

$$\frac{\boldsymbol{F}}{\rho} = -2\boldsymbol{\omega} \times \boldsymbol{v} - \boldsymbol{\omega} \times (\boldsymbol{\omega} \times \boldsymbol{r}), \tag{12}$$

where $\boldsymbol{r}$ is the radius vector from the rotation center and $\boldsymbol{\omega}$ is the angular velocity vector.

It assumes that the fictitious force only includes steady angular velocity, which may not allow us to compute the impulsive rotation case. The fictitious forces are taken into account for the collision and streaming process at each time step, which gives the general LBM formulation in the non-inertial reference axis,[24]

$$\begin{aligned}
& f_i(\boldsymbol{x} + \boldsymbol{c}_i\Delta t, t_n + \Delta t) \\
&= f_i(\boldsymbol{x}, t_n) - \frac{\Delta t}{\tau}(f_i(\boldsymbol{x}, t_n) - f_i^{eq}(\boldsymbol{x}, t_n)) + \left(1 - \frac{\Delta t}{2\tau}\right) S_i \\
&= f_i(\boldsymbol{x}, t_n) - \frac{\Delta t}{\tau}(f_i(\boldsymbol{x}, t_n) - f_i^{eq}(\boldsymbol{x}, t_n) + \frac{1}{2}S_i) + S_i \\
&= f_i(\boldsymbol{x}, t_n) - \frac{\Delta t}{\tau} f_i^{neq}(\boldsymbol{x}, t_n) + S_i.
\end{aligned} \tag{13}$$

This formulation has two particular features compared with the conventional formulation in the inertial frame [Eq. (1)]. One is that it requires a new definition of its macroscopic velocity for the equilibrium function and another is that it needs to employ the discrete forcing term S_i which will be detailed hereafter in Eq. (18).

First, the representative macroscopic velocity $\boldsymbol{v}$ has to be defined as considering the non-inertial acceleration. The velocity is designated as the one including half of the force, which is so called "half-force correction,"

$$\rho \boldsymbol{v}(\boldsymbol{x}, t_n) = \sum_i \boldsymbol{c}_i f_i(\boldsymbol{x}, t_n) + \frac{1}{2}\boldsymbol{F}(\boldsymbol{x}, t_n)\Delta t, \tag{14}$$

where $\boldsymbol{F}(\boldsymbol{x}, t_n)$ is a function of $\boldsymbol{\omega}$, $\boldsymbol{r}$, and $\boldsymbol{v}(\boldsymbol{x}, t_n)$, and density ρ is $\sum_i f_i(\boldsymbol{x}, t_n)$.

This new velocity is representative velocity at each discrete time step, which is applied to both the equilibrium function and discrete forcing term in Eq. (13). This treatment is essential to guarantee the second order accuracy in time and space discretization process through the trapezoidal rule.[22] Due to the external force $\boldsymbol{F}$ which is being acted on the fluid particles during the unit discrete time step, the macroscopic velocity $\boldsymbol{u}$ is also varied within the time step. It means that, over the discrete time step, the macroscopic velocity would be laid on somewhere between the pre-collide velocity and the velocity after adding the fictitious acceleration. Therefore, this half-force corrected macroscopic value $\boldsymbol{v}$ could be considered as the average velocity within the discrete time step, by which the discrete forcing scheme becomes more robust.

However, when the external force includes the Coriolis force which consists of the velocity, the force becomes a function of time which gives the implicit problem.[25–27] $\boldsymbol{v}(\boldsymbol{x}, t_n)$ is composed of $\boldsymbol{F}(\boldsymbol{x}, t_n)$ which is a function of $\boldsymbol{v}(\boldsymbol{x}, t_n)$ itself. One solution is to predict the force $\boldsymbol{F}(\boldsymbol{x}, t_n)$ from the post-collide discrete force of the previous time step $\boldsymbol{F}(\boldsymbol{x}, t_{n-1} + \frac{\Delta t}{2})$ by solving Eq. (15). Its solution is given as Eq. (16),

$$\frac{d\boldsymbol{a}}{dt} = -2\boldsymbol{\omega} \times \boldsymbol{a}, \tag{15}$$

$$\begin{aligned}\frac{\boldsymbol{F}(\boldsymbol{x}, t_n)}{\rho} = \begin{bmatrix} a_x(\boldsymbol{x}, t_n) \\ a_y(\boldsymbol{x}, t_n) \\ a_z(\boldsymbol{x}, t_n) \end{bmatrix} &= \begin{bmatrix} \cos(\omega\Delta t) & \sin(\omega\Delta t) & 0 \\ -\sin(\omega\Delta t) & \cos(\omega\Delta t) & 0 \\ 0 & 0 & 1 \end{bmatrix} \\ &\times \begin{bmatrix} a_x\left(\boldsymbol{x}, t_{n-1} + \dfrac{\Delta t}{2}\right) \\ a_y\left(\boldsymbol{x}, t_{n-1} + \dfrac{\Delta t}{2}\right) \\ a_z\left(\boldsymbol{x}, t_{n-1} + \dfrac{\Delta t}{2}\right) \end{bmatrix}, \quad \boldsymbol{\omega} = \omega\hat{z}, \end{aligned} \tag{16}$$

where Δt is the difference between t_n and t_{n-1}.

Then, the predicted external force at the current time step $\boldsymbol{F}(\boldsymbol{x}, t_n)$ could be applied to compute the half-force corrected velocity $\boldsymbol{v}(\boldsymbol{x}, t_n)$ in Eq. (14). Finally, this velocity satisfies the fictitious force equation as follows:

$$\frac{\boldsymbol{F}(\boldsymbol{x}, t_n)}{\rho} = -2\boldsymbol{\omega} \times \boldsymbol{v}(\boldsymbol{x}, t_n) - \boldsymbol{\omega} \times (\boldsymbol{\omega} \times \boldsymbol{r}). \tag{17}$$

Subsequently, the next question is how to impose the defined fictitious force on the fluid particles during the collision and streaming process. The following discrete forcing term (so called "Guo's forcing scheme") is chosen to enforce the fictitious forces on the particles at each collision and streaming step:[24]

$$S_i = w_i\left[\frac{\boldsymbol{c}_i - \boldsymbol{v}}{c_s^2} + \frac{(\boldsymbol{c}_i \cdot \boldsymbol{v})}{c_s^4}\boldsymbol{c}_i\right] \cdot \boldsymbol{F}. \tag{18}$$

This equation could recover the Navier–Stokes equation considering the discrete lattice effect[24] and also it removes unphysical dissipation in time-dependent incompressible flows.[27]

In the following, the HRR collision equation is to be set up including the discrete forcing term. The equation is transformed from general collision equation (13). The pre-collision distribution function $f_i(\boldsymbol{x}, t_n)$ in Eq. (13) does not include the half-force correction according to its original definition.[24] Therefore, the pre-collision distribution function in the HRR collision f_i^{HRR} should also be defined as excluding the half-force correction,

$$\begin{aligned} f_i^{HRR} &= f_i^{eq}\left(\boldsymbol{v} - \frac{1}{2}\boldsymbol{F}\Delta t\right) + f_i^{neq,HRR} \\ &= f_i^{eq}(\boldsymbol{v}) - 0.5S_i + f_i^{neq,HRR} + O(u^3)\,, \end{aligned} \tag{19}$$

where the half-force corrected macroscopic velocity $\boldsymbol{v}$ is applied to define the equilibrium function, discrete forcing term [Eq. (18)], and the non-equilibrium part [Eq. (3)] in the rotating mesh, and hence the scheme could maintain consistency. Since the orders of the equilibrium function and discrete forcing term are different, it comes with an $O(u^3)$ error, but this error is not corrected here, as the third order term is often neglected to recover the isothermal Navier–Stokes equation.

Finally, given Eqs. (13) and (19), the HRR collision equation in the non-inertial reference frame is derived as

$$\begin{aligned} f_i^{*,HRR} &= (f_i^{eq} - 0.5S_i) + f_i^{neq,HRR} - \frac{\Delta t}{\tau}f_i^{neq,HRR} + S_i + O(u^3) \\ &= f_i^{eq} + \left(1 - \frac{\Delta t}{\tau}\right)f_i^{neq,HRR} + 0.5S_i. \end{aligned} \tag{20}$$

It gives the final form of the HRR collision equation under the external force, which describes how the collision of the HRR model should occur in the non-inertial rotating frame.

B. Rotating to fixed grid interpolation

To transfer information from moving to fixed grids, the mesh velocity ($\boldsymbol{\omega} \times \boldsymbol{r}$ in the case of the rotating mesh) is first added to the macroscopic velocity in the moving grid (see Algorithm 1). This treatment is not needed for the non-equilibrium tensors because the mesh rotation does not affect the shear stress if the mesh rotates with a uniform angular velocity. The macroscopic values are then interpolated from the moving grid to the fixed grid. The boundary nodes of the fixed grid (black circles of the yellow fixed grid in Fig. 1) receive the data from the surrounding moving nodes. The interpolation scheme takes four moving nodes enclosing one target fixed node at the boundary (Fig. 2). Two different interpolation schemes are considered in this research. The bi-linear interpolation used here consists in linear interpolations by using the distances between the target node and input interpolating nodes, see Eq. (30).[28] This interpolation scheme is of second order of accuracy which is demonstrated through the Taylor expansion.[29] Also, the gradient based second order interpolation is tested.[30] The second order interpolation is built using the gradients, and hence the interpolation stencil is not larger than in the case of the

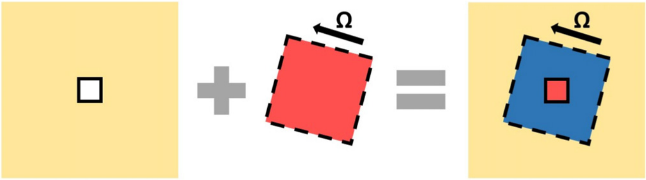

FIG. 1. Schematic diagram of the overset grids: fixed grid (yellow), rotating grid (red), overset region (navy), interpolation border from rotating to fixed grid (solid line), and interpolation border from the fixed to rotating grid (dashed line).

bilinear interpolation which contributes to reduce the computational cost. More details are described in Sec. IV C.

This interpolation is performed separately for each macroscopic variable such as velocity, density, and non-equilibrium tensor Π_{neq}. Here, the non-equilibrium tensor is computed as being described in Eqs. (4) and (7). The next step is to redefine the vectors of the interpolated macroscopic values according to the fixed reference axis, through the rotation matrix R. Finally, the equilibrium and non-equilibrium distribution functions at the fixed node are reconstructed from the interpolated macroscopic values by using the Hermite polynomials according to formulas (10) and (8).

ALGORITHM 1. Interpolation from rotating to fixed grid.

```
for all border nodes at fixed grid do
    for 4 surrounding interpolating nodes at moving grid do
        $\hat{\boldsymbol{u}}_{mg} = \boldsymbol{u}_{mg} + \boldsymbol{\omega} \times \boldsymbol{r},\ \hat{\Pi}_{neq,mg} = \Pi_{neq,mg}$;
        $\rho_{fg} = I(\rho_{mg}),\ \hat{\boldsymbol{u}}_{fg} = I(\hat{\boldsymbol{u}}_{mg}),\ \hat{\Pi}_{neq,fg} = I(\hat{\Pi}_{neq,mg})$: interpolate macroscopic values from moving to fixed grid;
    end
    $\boldsymbol{u}_{fg} = R(\hat{\boldsymbol{u}}_{fg}),\ \Pi_{neq,fg} = R(\hat{\Pi}_{neq,fg})$: redefine macroscopic vectors from moving to fixed reference axis;
    $f_{i,fg} = \mathrm{g}(\rho_{fg}, \boldsymbol{u}_{fg}, \Pi_{neq,fg})$: reconstruct $f_{i,fg}$;
end
```

C. Fixed to rotating grid interpolation

The interpolation step from fixed to moving grid is similar to the previously described one, except for considering the half force correction at the end of the interpolation procedure (see Algorithm 2). First, macroscopic values of the fixed grids are projected on the moving grid by using the interpolation [Eq. (30) or Eq. (31)], based on four fixed nodes surrounding one target moving node (Fig. 2, right). Each macroscopic term is transferred through the interpolation separately, such as ρ, $\boldsymbol{u}$, and Π_{neq}. Then, the next step is to transform the reference axis of the interpolated macroscopic values using the rotation matrix R. Additionally, the mesh velocity has to be subtracted. Note that no extra treatment is needed for the non-equilibrium tensors because the mesh rotation does not affect the shear stress if the mesh rotates with a uniform angular velocity. Next, the distribution functions at the border of the moving grid are reconstructed from the interpolated macroscopic values, by expanding the equilibrium and non-equilibrium distribution functions through the Hermite polynomials, see Eqs. (10) and (8). Finally, half of the body forces are subtracted from the reconstructed distribution functions. The macroscopic momentum flux in the moving region contains half of the force, while its distribution function does not, see Eq. (14).[24] Therefore, this subtraction is to recover the distribution functions before undergoing the half-force correction.

ALGORITHM 2. Interpolation from fixed to rotating grid.

```
for all border nodes at moving grid do
    for 4 surrounding interpolating nodes at fixed grid do
        $\rho_{mg} = I(\rho_{fg}),\ \tilde{\boldsymbol{u}}_{mg} = I(\boldsymbol{u}_{fg}),\ \tilde{\Pi}_{neq,mg} = I(\Pi_{neq,fg})$: interpolate macroscopic values from fixed to moving grid;
    end
    $\hat{\boldsymbol{u}}_{mg} = R(\tilde{\boldsymbol{u}}_{mg}),\ \hat{\Pi}_{neq,mg} = R(\tilde{\Pi}_{neq,mg})$: redefine macroscopic vectors from moving to fixed reference axis;
    $\boldsymbol{u}_{mg} = \hat{\boldsymbol{u}}_{mg} - \boldsymbol{\omega} \times \boldsymbol{r},\ \Pi_{neq,mg} = \hat{\Pi}_{neq,mg}$;
    $\hat{f}_{i,mg} = \mathrm{g}(\rho_{mg}, \boldsymbol{u}_{mg}, \Pi_{neq,mg})$: reconstruct $\hat{f}_{i,mg}$;
    $f_{i,mg} = \hat{f}_{i,mg} - F_i/2$: "half-force correction;"
end
```

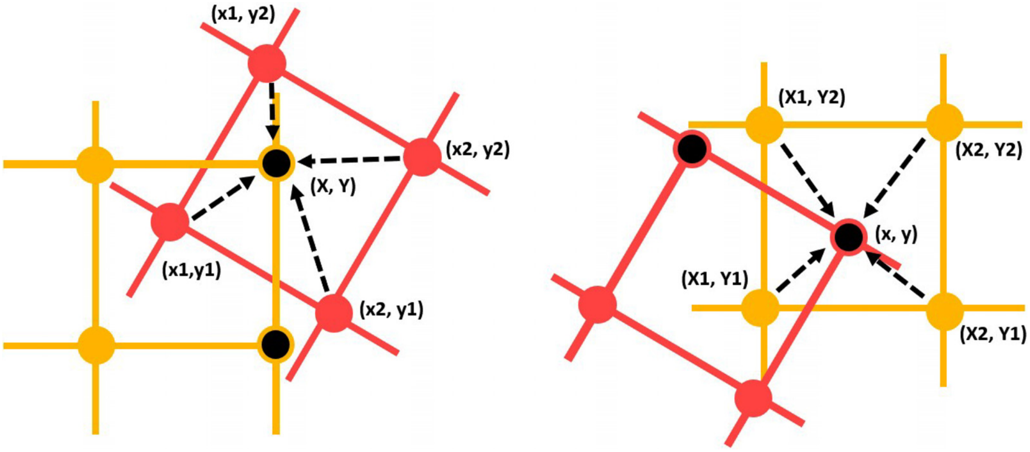

FIG. 2. Schematic diagram of the bi-linear interpolation between the moving (red) and fixed (yellow) grids. Left: moving to fixed grid interpolation. Right: fixed to moving grid interpolation. The nodes at the boundary of each grid receive the data from the other grid (black circle).

D. Boundary condition at solid walls

The extrapolation-based boundary condition is applied on the rotating solid wall.[31,32] The method reconstructs the distribution functions of the boundary nodes using the target macroscopic values at the exact location of the wall and the nearest fluid nodes.[32] Therefore, the method can describe the curved wall without facing the "staircase approximation" problem while having the second order accuracy.[31] Since the overset rotating grid and its non-inertial rotating reference axis are attached to the rotating solid body as moving together, this boundary condition has exactly the same performance as the conventional one in the fixed grid. As a matter of fact, it does not face any issue with the moving boundary coming from redefining the fluid and solid nodes at each time, such as methods using ghost-cells[33,34] or immersed boundary methods.[5,11]

IV. ACCURACY OF THE OVERSET LRF–HRR ALGORITHM

A. Accuracy of the discrete forcing term on the HRR model

The accuracy of the overset LRF method can be evaluated by comparing the obtained flow fields with those of the reference computation without overset grids. There are two main major sources of error. The first one is located near the border of overset grids, where spurious numerical effects are observed due to the interpolation scheme itself, and consequently the reconstruction step which is performed afterwards to compute the macroscopic variables. The second source of error is related to the discrete forcing term present inside the rotating region to account for the non-inertial rotating reference axis.

A second order discrete forcing scheme is reliable and robust enough to achieve the second-order accuracy.[22,24] However, it is an extra source of error which adds on the interpolation error. In particular, for uniform and incompressible flows, this error from the discrete forcing term inside the rotating region becomes dominant compared to the interpolation error, because the bi-linear interpolation scheme is exact for a uniform flow field, in a sense that its interpolation error becomes negligible as the second order derivatives of the perturbation, and also, the error due to the reconstruction of the non-equilibrium part is negligible for incompressible flows. For instance, in the case of the arbitrary Lagrangian–Eulerian method (ALE) where no discrete forcing term is used, the error is uniquely created by the interpolation and reconstruction process at the borders and gives a trivial value of 10^{-14} for an incompressible uniform flow.[35] Therefore, considering the simple configuration of uniform flow is a relevant way to isolate the effect of the forcing term and analyze its error on the global overset LRF method.

The forcing term generates two kinds of error: the discretization of the forcing scheme in time and space, and the error due to the weakly compressible approximation. First, the classically used trapezoidal rule to integrate in time and space LBM equations with discrete forcing terms is generating second-order discretization error $O(\Delta x^2)$ [Eq. (21)].[22,36] Also, the compressibility error $O(Ma^2)$ comes from gradients of force fields which have $O(Ma^2)$ error when the force fields are the fictitious forces [see Eq. (21)].[36,37] These errors are added to the conventional compressibility error $O(Ma^2)$ which occurs in the lattice even without the force fields, but becoming more dominant according to the rotation speed [see Eq. (21)],[38–41]

$$\frac{\partial(\rho u_\alpha)}{\partial t} + \partial_\beta(c_s^2 \rho \delta_{\alpha\beta} + \rho u_\alpha u_\beta) = \partial_\beta \Pi^{(1)}_{\alpha\beta} + F_\alpha + O(\Delta x^2, Ma^2). \tag{21}$$

Figure 3 (left) shows the discretization error of the discrete forcing term, using the L2 norm of the error defined by

$$E_F = \sqrt{\frac{\sum (F - F_{exact})^2}{\sum F^2_{exact}}}, \tag{22}$$

where F_{exact} is the analytical forcing term.

The error is measured in the overset rotating grid of the LRF simulation. A uniform channel flow has low Reynolds number $Re = \frac{U_0 L}{\nu} = 60$, where L is the channel height, and inlet Mach number $Ma_0 = 0.17$. The number of lattices in the channel height is N_x which increased from 50 to 125. The error is reduced as the number of lattice points is increased, following a second-order accuracy trend. This mesh convergence test is conducted based on the acoustic scaling.[42] Also, it is shown that accuracy with the HRR collision model always outperforms that of the BGK collision model. Here, the BGK collision

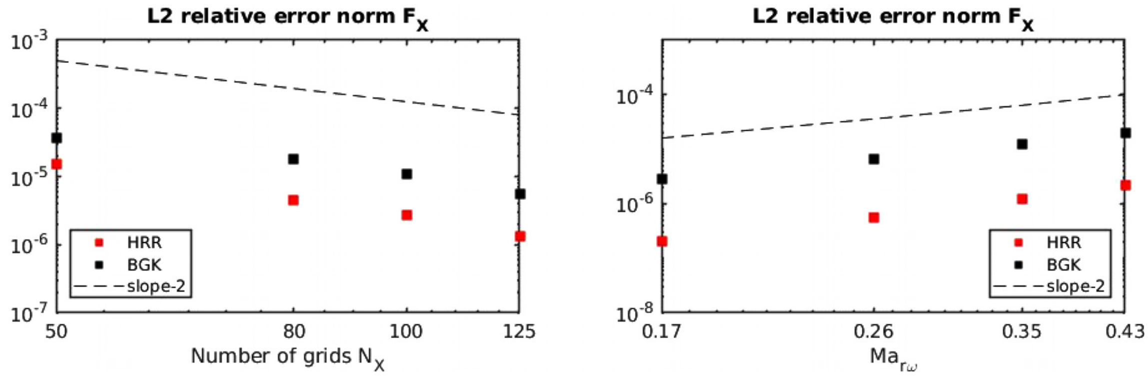

FIG. 3. Relative L2 error norm of the discrete forcing term F_x in the overset rotating grid. The error is calculated from the analytical force. Left: mesh convergence test at the rotation speed $Ma_{r\omega} = 0.17$. Right: compressibility error at different mesh rotation speeds with the number of lattices $N_x = 200$. In the legend, "slope-2" indicates the second-order accuracy trend.

model uses the same equilibrium function as for the HRR. Figure 3 (right) shows the compressibility error on the discrete forcing term at different rotation speeds. The mesh resolution is set high enough ($Nx = 200$) to minimize as much as possible the error due to the spatial discretization. The Mach number represents the rotation speed at the edge of the rotating square mesh: $Ma_{r_\omega} = \frac{r\omega}{c_s}$, with r referring to half length of the rotating square. The results show the second-order accuracy, which highlights the compressibility error by using the discrete forcing term in the overset rotating grid.

Given the fact that major differences between the BGK and HRR models are used to define the non-equilibrium parts, analyzing the spurious error of the non-equilibrium tensor can be helpful to figure out the improvement made by the HRR model. Using multi-scale analysis, it becomes easier to understand the connection between the effect of the different collision models and the accuracy of the discrete forcing term.[24,27,43] From the Chapman–Enskog expansion, the transport equations of macroscopic values can be derived from the lattice Boltzmann distribution functions at each different space and time scales. In the first order time and space scale where $\mathrm{t} = \varepsilon t_1$ and $\mathrm{x} = \varepsilon x_1$, the continuity and Euler equations are recovered,[24,27,43]

$$\frac{\partial \rho}{\partial t_1} + \nabla_1 \cdot (\rho u_\alpha) = 0, \tag{23}$$

$$\frac{\partial (\rho u_\alpha)}{\partial t_1} + \nabla_1 \cdot (c_s^2 \rho \delta_{\alpha\beta} + \rho u_\alpha u_\beta) = F_{1\alpha}. \tag{24}$$

Note the presence of the forcing term in the Euler equation [Eq. (24)] affecting the momentum transport $\rho \boldsymbol{u}$. In the second order time scale where $\mathrm{t} = \varepsilon t_2$, the equations read[24,27,43]

$$\frac{\partial \rho}{\partial t_2} = 0, \tag{25}$$

$$\frac{\partial (\rho u_\alpha)}{\partial t_2} = \nabla_1 \cdot \Pi^{(1)}_{\alpha\beta}. \tag{26}$$

The momentum transport equation [Eq. (26)] is driven by the shear stress, thus showing that accuracy of the forcing term is connected to the non-equilibrium tensor through the mass flux in different time scales. This implies the possibility that accuracy of the discrete forcing term can be improved by reducing the spurious errors of the non-equilibrium tensor. The error on the non-equilibrium tensor is measured in the overset rotating grid of the LRF simulation. It is shown in Fig. 4 for different collision models BGK and HRR, by computing the L2-norm of the error as follows:

$$E_\Pi = \sqrt{\frac{\sum (\Pi^{neq} - \Pi^{neq}_{ref})^2}{N}}, \tag{27}$$

where Π^{neq}_{ref} is the non-equilibrium tensor of reference simulation with the single fixed grid.

Without the overset rotating grid, the reference non-equilibrium tensor is zero at machine accuracy 10^{-15} for both BGK and HRR collision models. Indeed, the shear stress and divergence are supposed to vanish in this low Reynolds number and low Mach regime of uniform channel flow, but they appear in the overset LRF simulation due to the defect of its algorithm. It shows that the HRR collision model clearly has less spurious error in the non-equilibrium tensor compared to the BGK, from which we may deduce the capability of the HRR collision model to recover more accurate non-equilibrium tensor in the overset LRF method, thus enhancing accuracy of the discrete forcing term in the rotating region. The mechanism driving how the HRR model dissipates the spurious modes is studied using linear stability analysis.[9]

The improvement achieved by the HRR model is more clearly visualized in high Reynolds number flow. Figure 5 left shows the velocity field without the overset rotating grid. The inlet Mach number is $Ma_0 = 0.17$ and the Reynolds number is set to $Re = 10^7$. It shows that the flow fields remain stable both with the BGK and HRR collision operators. However, when the non-inertial rotating grid is overset, the flow field computed with the BGK collision operator becomes unstable and gives rise to spurious fluctuations (Fig. 5, middle). The numerical errors implied by the fictitious force and high local Mach number in the rotating region induce instability on the field, which the BGK collision operator cannot damp. By contrast, the flow field computed with the HRR collision operator stays stable in high Reynolds number flow (Fig. 5, right). More detailed analysis is delivered subsequently in Sec. V A.

B. Impact of σ on the overset local reference frame

The HRR model adopts two different ways to constitute the non-equilibrium distribution functions. First, it projects the non-

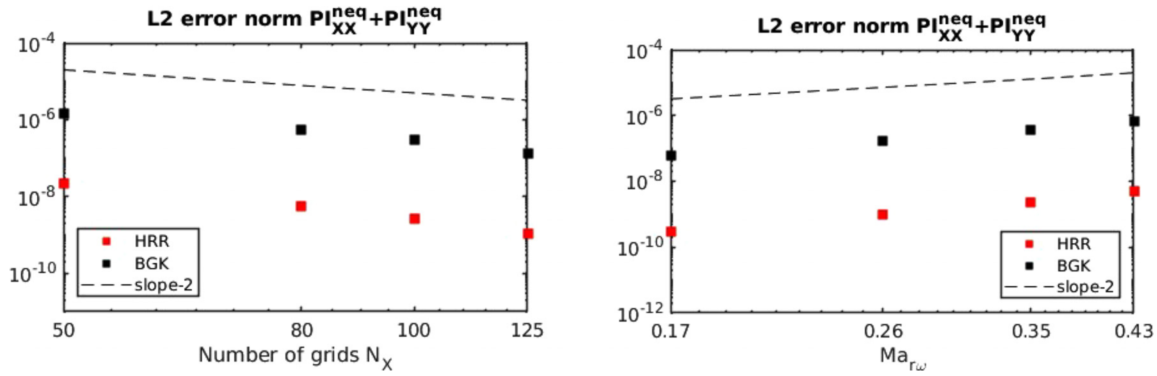

FIG. 4. L2 error norm of the non-equilibrium tensor $\Pi^{neq}_{XX} + \Pi^{neq}_{YY}$ in the overset rotating grid. The error is calculated from the analytical value. Left: mesh convergence test at the rotation speed $Ma_{r\omega} = 0.17$. Right: compressibility error at different mesh rotation speeds using $N_x = 200$.

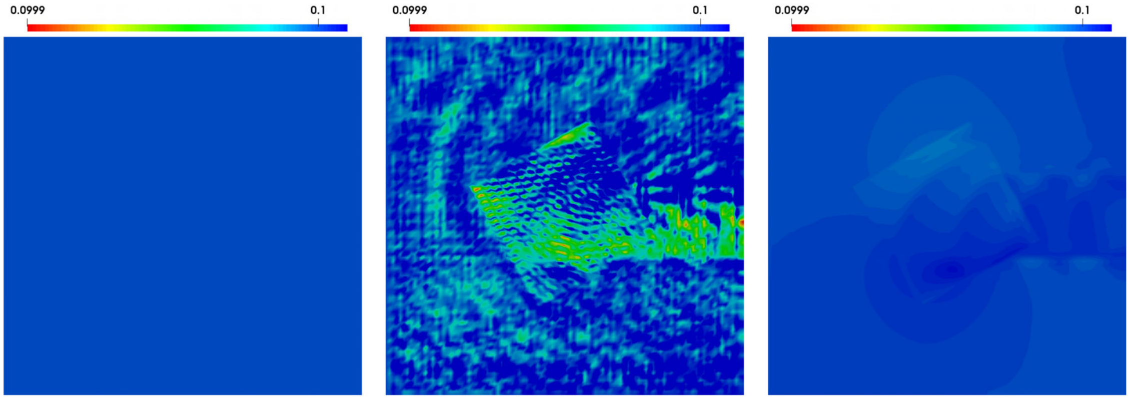

FIG. 5. Velocity fields in uniform channel flow with $Re = 10^7$ and $Ma_0 = 0.17$. Left: normal fixed grid (both the BGK and HRR models). Middle: the overset LRF grid with the BGK model. Right: the overset LRF grid with the HRR model.

equilibrium functions onto the low order Hermite polynomials, by which only the essential low order non-equilibrium tensors are able to be preserved. Also, it uses the stresses computed by finite difference schemes, which are applied to reconstruct the low order non-equilibrium parts.

An interesting consequence of computing these stresses using finite difference schemes is that artificial viscosity is injected in the flow, which may be related to the error terms coming out of the truncation and modeling errors,[4]

$$\begin{aligned} S^{HRR} &= S + \Delta S^{FD} + \Delta S^{LBM} \\ &\simeq S + (1-\sigma)\frac{1}{2}\left(\frac{1}{6}\Delta x^2(\partial_\alpha^3 u_\beta + \partial_\beta^3 u_\alpha)\right) + \sigma O(\Delta x^2, u^3). \end{aligned} \tag{28}$$

S is the exact shear strain. The strain calculated by the finite difference S^{FD} gives a discretization error ΔS^{FD} compared to the exact shear strain.[4] Also, the strain ΔS^{LBM} calculated by the second order momentum of the non-equilibrium distribution function contains an $O(u^3)$ error relative to the exact shear strain.[41,44,45] This alternative way of defining the shear stress brings about the artificial viscosity, which may contribute to improving the stability.[4,8,9]

Although the artificial viscosity of the scheme damps the ghost mode carrying non-physical information, there also exists possibility of over-damping the physical modes, as it behaves like physical viscosity in the fluid flow.[8,46,47] Therefore, it is better to control the use of σ once the stability is achieved to prevent the over-damping. This stabilization mechanism has been extensively analyzed using linear stability analysis to show how σ can kill the non-physical modes.[8]

The effect of σ on the overset LRF algorithm is studied on Poiseuille channel flow configuration by comparing with the reference fixed case. The Reynolds number is set to $Re = \frac{U_0 L}{\nu} = 500$, where L is the channel height, the inlet Mach number is $Ma_0 = 0.17$, and the non-dimensional relaxation time is set to $\tau = \frac{\nu}{c_s^2 \Delta t} + \frac{1}{2} = 0.56$. The number of lattices in the channel height is varied as $N_x = 100, 125, 160, 200$. The empty rotating mesh is rotated with angular velocity ω. The rotation speed is represented by the local Mach number at the edge of the rotating grid $Ma_{r\omega} = \frac{r\omega}{c_s}$, where r is half length of the rotating grid. Figure 6 shows the error in the velocity field using the L2-norm of the error computed by

$$E_u = \sqrt{\frac{\sum (u - u_{ref})^2}{\sum u_{ref}^2}}, \tag{29}$$

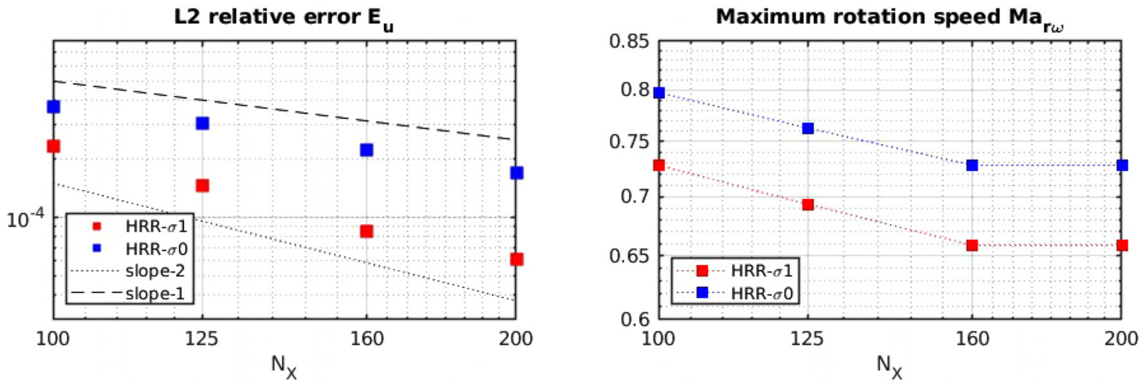

FIG. 6. Results obtained with the overset method at various parameters σ of the HRR model in $Re = 500$, $Ma_0 = 0.17$. Left: L2 relative velocity error with $Ma_{r\omega} = 0.347$. Right: maximum rotation speed of the overset rotating mesh at which numerical stability is preserved.

where u_{ref} is the velocity field with the HRR model in the reference fixed grid.

The numerical errors between the overset LRF-HRR and reference HRR simulations are computed by varying the parameter σ at a different number of lattices. Both the overset and reference simulations use the same σ values for the matter of consistency. Figure 6 (left) shows that this numerical error on the fluid velocity is increased with $\sigma = 0$, indicating that the order of accuracy of the overset algorithm is reduced. By contrast, Fig. 6 (right) shows that the maximum rotation speed of the overset rotating grid is increased for $\sigma = 0$. It means that the method can achieve more stability by compensating the accuracy, but the detailed analysis of this mechanism is left for future works. Therefore, in this research, $\sigma = 1$ is maintained to keep the second order of accuracy for the overset method, except for the vortex advection test case (Sec. V B) where it is shown that a slight amount of $\sigma = 0.995$ can suppress the spurious noise while not corrupting pressure profile. In Fig. 6 (right), the maximum rotation speed is measured as the limit where the simulation is numerically stable, and hence it does not guarantee the accuracy near this limit due to the error coming from the high Mach number.

C. Effect of different interpolation methods on the overset method

Two different interpolation methods are considered, namely, the bi-linear interpolation and the gradient-based quadratic Hermite interpolation. The bi-linear interpolation is composed of two sets of linear interpolations in each dimension by using the four neighboring nodes, which is proven to have the second order of accuracy based on the Taylor expansion.[29] Therefore, it is enough to recover the second order discretization error of the LBM scheme. However, the leading order of interpolation error is $O\left(\frac{\partial^2 \rho u}{\partial x^2}\right)$ which corresponds to the spurious viscosity.[48] It could affect the simulation if one needs to recover sensitive parameters such as the acoustic properties. The bilinear interpolation is constituted as follows:[28]

$$M(X,Y) = \frac{1}{(x_2 - x_1)(y_2 - y_1)} \begin{bmatrix} x_2 - X, & X - x_1 \end{bmatrix} \times \begin{bmatrix} \tilde{M}(x_1, y_1) & \tilde{M}(x_1, y_2) \\ \tilde{M}(x_2, y_1) & \tilde{M}(x_2, y_2) \end{bmatrix} \begin{bmatrix} y_2 - Y \\ Y - y_1 \end{bmatrix}, \tag{30}$$

where each coordinate follows the description of Fig. 2.

The second order interpolation can overcome this issue as suppressing the numerical error.[30] The method has a third order accuracy, found by Taylor expansion.[30] The leading order of the error is reduced to the third derivative of the equilibrium function $O\left(\frac{\partial^3 f^{eq}}{\partial x^3}\right)$.[48] Since the leading order of the interpolation is not similar to the numerical viscosity anymore, it appears more appropriate to study sensitive parameters, such as acoustic properties. The gradient based second order interpolation scheme is employed which constitutes the second order interpolation equation by using velocities and gradients of the neighboring nodes.[30] Using the gradients makes the scheme more compact, using only the four neighboring nodes, and thus saving computational time as the solver already stores information about the gradients for certain purposes such as post-processing and constituting turbulence model,

$$\begin{aligned} u(x', y') &= a_0 + a_1 x' + a_2 y' + a_3 x' y' + c_x(1 - x'^2) + c_y(1 - y'^2), \\ v(x', y') &= b_0 + b_1 x' + b_2 y' + b_3 x' y' + d_x(1 - x'^2) + d_y(1 - y'^2), \end{aligned} \tag{31}$$

where all the coefficients a_i, b_i, c_i, and d_i and coordinate x' and y' are defined in Ref. 30. The coefficients a_i and b_i concern velocities in the neighboring nodes, while c_i and d_i concern the gradients.

Two different interpolation methods are tested in the case of Poiseuille flow. The inlet Mach number is $Ma_0 = 0.17$. The number of lattices in each dimension is $N_L = 100$. The Reynolds number is $Re = \frac{U_0 L}{\nu} = 500$. The overset rotating mesh is square shaped which has 40 lattices in its length $N_{L'} = 40$. The local Mach number at the edge of the overset rotating mesh is $Ma_{r\omega} = \frac{L'/2\omega}{c_s} = 0.347$. The setup is presented in Fig. 7.

Spurious error of the overset method is analyzed by subtracting the flow field from the reference simulation which is made from the single fixed grid. Spurious velocity field is generated from the interpolation boundary and the error is reduced by increasing the order of interpolation scheme (Fig. 8). Also, spurious radiated noise is studied by analyzing the pressure fluctuation $\left|\frac{\partial p}{\partial t} - \frac{\partial p_{ref}}{\partial t}\right|$ in Fig. 9. It shows that the spurious noise is generated from the interpolation boundary and then, it propagates through the field. The second order interpolation suppresses the noise more effectively. The errors are listed in Table I.

This brings about two conclusions. First, the second order interpolation guarantees more accurate performance compared to the linear interpolation, though the linear interpolation has an $O(\Delta x^2)$ error term which is enough to recover the second order discretization error of the LBM scheme. Also, the bi-linear interpolation gives the numerical error with a leading order $O\left(\frac{\partial^2 \rho u}{\partial x^2}\right)$ which corresponds to spurious viscosity. Therefore, the second order interpolation is recommended if one is interested in viscosity-sensitive parameters, such as acoustic properties and turbulence. In this work, the second order interpolation is tested for the vortex advection (Sec. V B) and 3D large-eddy simulation of the turbulent flow around a rotating cylinder (Sec. V E).

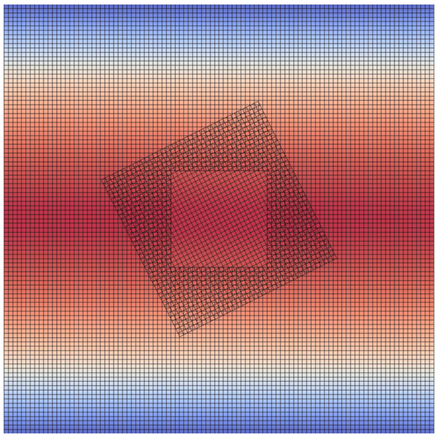

FIG. 7. Overset grids for the Poiseuille flow. The rotating grid is superposed on the fixed grid. The fixed grid has a void in the middle.

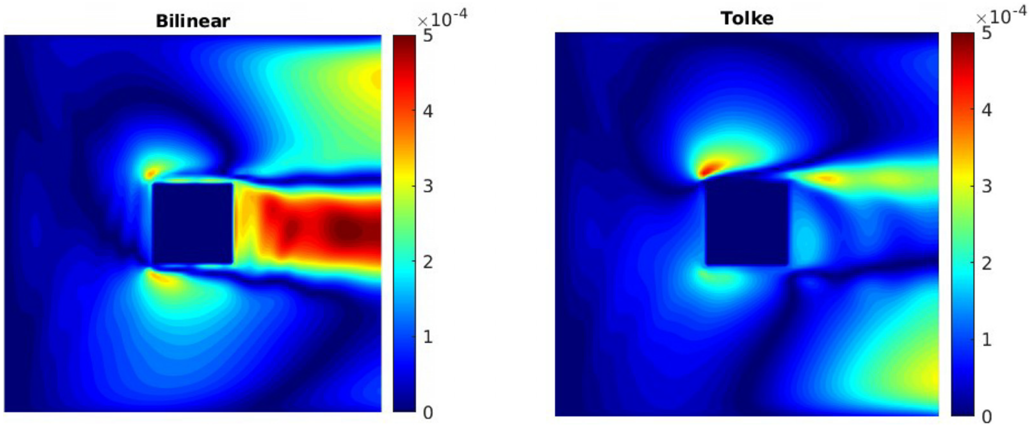

FIG. 8. Instantaneous spurious velocity fields of the overset grids in the Poiseuille flow. The spurious errors are defined as $|u - u_{ref}|/u_0$, where u_0 is the maximum velocity. Left: bi-linear interpolation. Right: second order interpolation. The reference simulation is computed in the normal fixed grid.

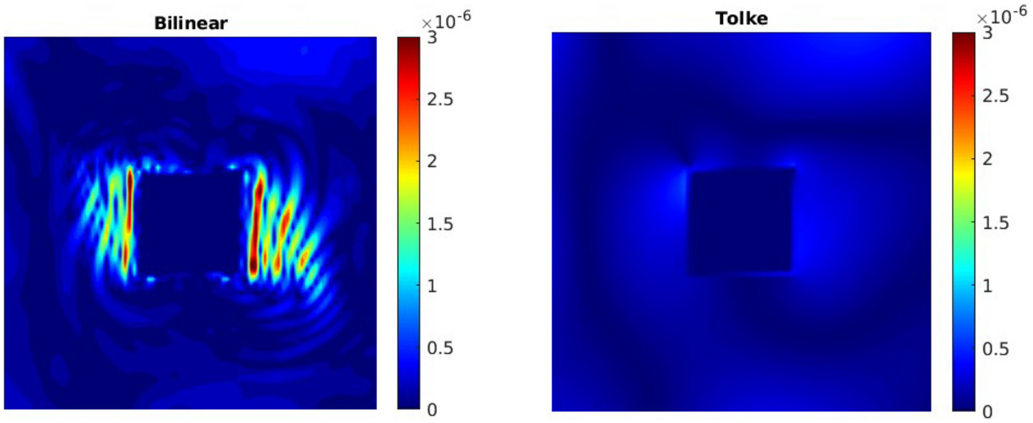

FIG. 9. Instantaneous spurious noise fields of the overset grids in the Poiseuille flow. The spurious errors are defined as $|\frac{\partial p}{\partial t} - \frac{\partial p_{ref}}{\partial t}|$. Left: bi-linear interpolation. right: second order interpolation. The reference simulation is computed in the normal fixed grid.

V. NUMERICAL VALIDATION OF THE OVERSET LRF–HRR ALGORITHM

A. High Re uniform channel flow without solid body

The first test case consists in a simple uniform channel flow. The empty rotating mesh is overset on the fixed mesh to simulate the uniform flow without any solid body. To produce the reference data, the single fixed mesh is set up to simulate the same uniform channel flow. The Reynolds number of the flow ($Re = \frac{U_0 L}{\nu}$) is set to 10^7 and the inlet Mach number is $Ma_0 = 0.17$. There are 100 lattices in the length of the channel $L = 100\Delta x$. The overset rotating mesh is square shaped which has 40 lattices in its length $L' = 40\Delta x$. The local Mach number at the edge of the overset rotating mesh is $Ma_{r\omega} = \frac{L'/2\omega}{c_s} = 0.347$. The bilinear interpolation is applied in this section.

TABLE I. Error comparison between the bilinear and gradient-based second order Hermite interpolation.[30]

	Bilinear	Second order Hermite
E_u [a]	2.2399×10^{-4}	1.4931×10^{-4}
$E_{u,max}$ [b]	5.0805×10^{-4}	4.5188×10^{-4}
$E_{dp/dt}$ [c]	4.2036×10^{-7}	2.0317×10^{-7}
$E_{dp/dt,max}$ [d]	3.8406×10^{-6}	6.2729×10^{-7}

[a] L2 relative norm. Same as Eq. (29).
[b] Maximum error.
[c] L2 averaged norm. Same as Eq. (33) as being replaced by dp/dt.
[d] Maximum error.

Figure 10 shows the velocity error fields of the overset LRF simulations. The error fields are computed from the reference simulations with the single fixed grids ($|\frac{u-u_{ref}}{u_{ref}}|$). Both overset simulations are conducted with Guo's forcing scheme as described in Eq. (18). On the left side, the error field from the LRF simulation with the BGK collision model is plotted, exhibiting spurious oscillations due to the instability of the BGK collision model. By contrast, the HRR collision model can successfully kill the spurious instabilities generated by the LRF algorithm and stabilize the flow (Fig. 10, right). For a quantitative study, the L2 relative error norms between the overset LRF simulations and the reference simulations are computed as follows:

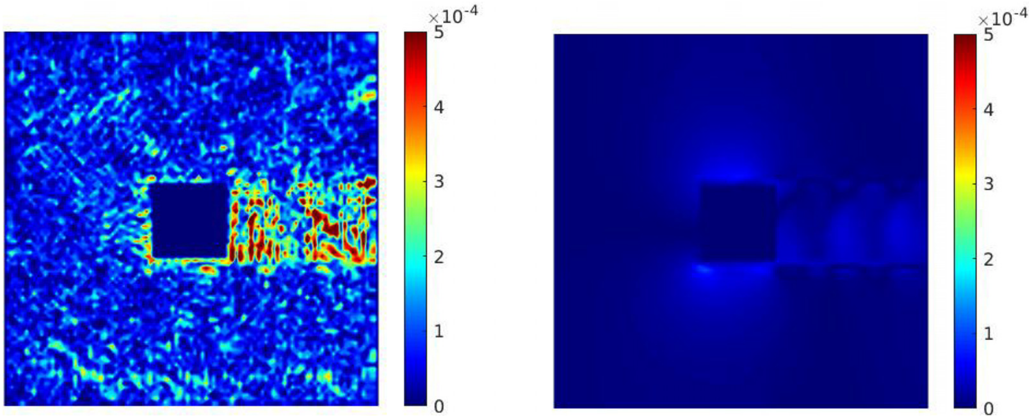

FIG. 10. The velocity error fields in the overset LRF simulations with the different collision models. Left: BGK model. Right: HRR model with $\sigma = 1.0$.

$$E_u = \sqrt{\frac{\sum (u - u_{ref})^2}{\sum u_{ref}^2}}. \tag{32}$$

Figure 11 shows that the L2 errors of the HRR collision models are smaller than the error of the BGK model which confirms the plots of Fig. 10. Also, both collision models are tested by using the forcing scheme proposed by He *et al.*[49] Different forcing terms are tested to show the robustness of the overset scheme. For both forcing schemes, the HRR-based overset methods have smaller error compared to the BGK-based overset methods.

Figure 12 shows the divergence error fields of the LRF domains with BGK and HRR collision models. The error fields are evaluated by subtracting the divergence fields of the LRF domains from those of the reference domains ($|\nabla \cdot \boldsymbol{u} - \nabla \cdot \boldsymbol{u}_{ref}|$). Both error fields are computed based on Guo's forcing scheme given in Eq. (18). The error field of the BGK collision model, which is the difference between the overset LRF–BGK and the reference BGK computations, shows spurious oscillations, which are reduced if the HRR collision model is used instead.

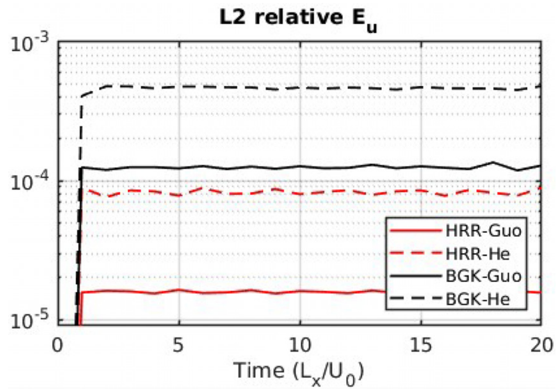

FIG. 11. L2 relative velocity error norms of the overset LRF simulations with the different collision models and discrete forcing scheme. The errors are evaluated during 20 flow through time ($20\ FFT = 20\frac{L_x}{U_0}$).

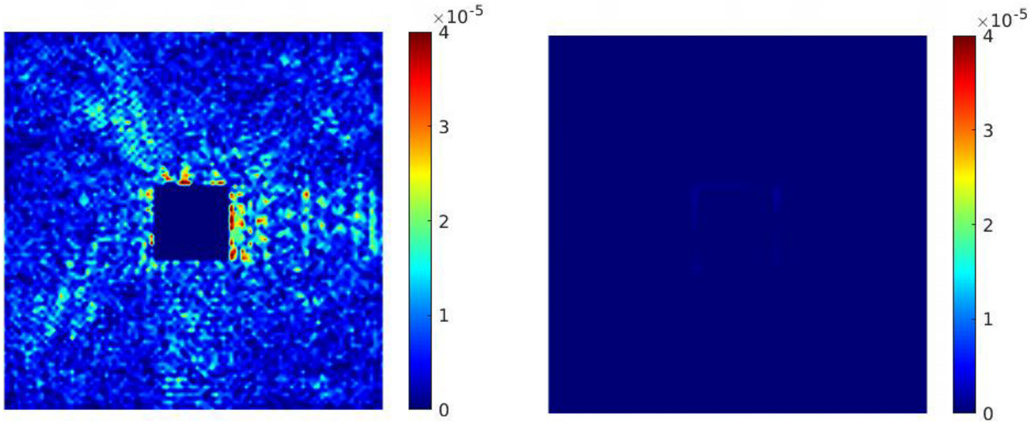

FIG. 12. The divergence error fields of the overset LRF simulations with the different collision models. Left: BGK model. Right: HRR model with $\sigma = 1.0$.

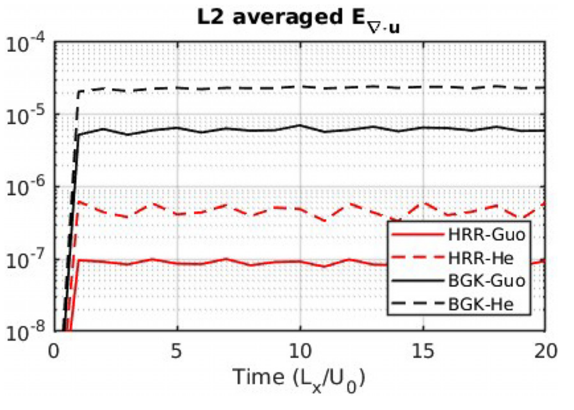

FIG. 13. L2 averaged divergence error norms of the overset LRF simulations with the different collision models and forcing schemes. The errors are evaluated during 20 FTT.

In Fig. 13, the errors are quantitatively expressed where the L2 averaged error norms are given as

$$E_{\nabla \cdot \boldsymbol{u}} = \sqrt{\frac{\sum (\nabla \cdot \boldsymbol{u} - \nabla \cdot \boldsymbol{u}_{ref})^2}{N}}. \tag{33}$$

It shows that the L2 error norm of the divergence is more reduced with the HRR collision model compared to the BGK collision model, while the error is bounded in time. In Fig. 13, apart from Guo's forcing scheme, He's forcing scheme is also tested to actualize the fictitious force inside the rotating region.[49] For both forcing schemes, the HRR based overset methods have smaller divergence errors compared to the BGK based overset methods. Considering the divergence is closely related to acoustic noises, and this implies that the HRR collision model can contribute to attenuating the spurious noises generated by the overset LRF mesh for industrial applications.

B. High Re vortex advection

A barotropic vortex passing through an overset rotating mesh is then tested, to identify how the overset method affects the vortex structure over time. The 2D vortex structure is defined by imposing initial velocity and density fields on the 2D computational domain with periodic boundaries. Once the simulation is started, the initial vortex structure keeps flowing through the computational domain, thanks to the periodic boundaries,

$$u_x = U_0 - \varepsilon \left(\frac{y - y_c}{R_{vortex}} \right) \exp\left[-\frac{(x - x_c)^2 + (y - y_c)^2}{2R_{vortex}^2} \right], \tag{34}$$

$$u_y = \varepsilon \left(\frac{x - x_c}{R_{vortex}} \right) \exp\left[-\frac{(x - x_c)^2 + (y - y_c)^2}{2R_{vortex}^2} \right], \tag{35}$$

$$\rho = \rho_0 \exp\left[-\frac{\varepsilon^2}{2c_s^2} \exp\left(-\frac{(x - x_c)^2 + (y - y_c)^2}{R_{vortex}^2} \right) \right]. \tag{36}$$

Equations (34) and (35) define the initial velocity fields of the vortex in 2D Cartesian coordinates, where U_0 is the uniform freestream velocity, which has the Mach number $Ma_0 = 0.17$, and ε refers to the vortex strength, which relates to the vortex rotation speed.[50] The vortex strength ε is set equal to 0.1, which implies the Mach number at the tip of the rotating vortex $Ma_{vortex} = \frac{\varepsilon}{c_s} = 0.17$. Hence, the velocity field of the vortex is defined by Ma_0 and Ma_{vortex}. The coordinate (x_c, y_c) is the location of vortex center. Also, Eq. (36) describes the density field of the vortex.[50] Note that this density field is for athermal conditions. Kinematic viscosity is set low to prevent the vortex structure from being dissipated due to the physical viscosity ($Re = \frac{2U_0 R_{vortex}}{\nu} = 10^{10}$). Figure 14 shows the density field of the vortex. The length of the whole computational domain is 20 times of the vortex radius $L_x = L_y = 20R_{vortex}$, where the number of lattices is $N_x = 200$. The length of the overset rotating domain is eight times of the vortex radius $L'_x = L'_y = 8R_{vortex}$, using 80 lattices. The angular velocity of the overset rotating grid ω is defined to have the local velocity at the edge of the overset rotating grid as $Ma_{r\omega} = \frac{\omega L'/2}{c_s} = 0.2$. The number of lattices in the radius of the vortex is set as $N_{vortex} = 10$.

When the vortex flows over the background fixed mesh, it penetrates through the overset rotating mesh in the middle. In this condition, there are two requirements to maintain the vortex structure over time: the first one is a low viscosity condition to prevent the vortex from being dissipated and the second one is accuracy of the LRF algorithm which generates numerical errors related to the discrete forcing term and interpolation between two grids (see Secs. III and IV A).

To evaluate the dissipation, the simulation results using the LRF algorithm are compared to reference test cases, obtained for a barotropic vortex simulated with the HRR model in the single fixed mesh, which is known to be stable.[6] Figure 15 shows that, as the vortex moves through the overset rotating mesh, the density profile is gradually smoothed. In this figure, the HRR models with $\sigma = 1$ are considered. It shows that the HRR methods perform better than the BGK model to preserve the density profile. Also, the second order interpolation is more robust compared to the bilinear interpolation because the spurious viscosity generated from the bilinear interpolation dissipates the vortex structure.[48] This dissipation is caused by the numerical defects of the overset LRF algorithm, which is quantified at different mesh resolutions (Fig. 16). The relative L2-norm of the error on pressure reads

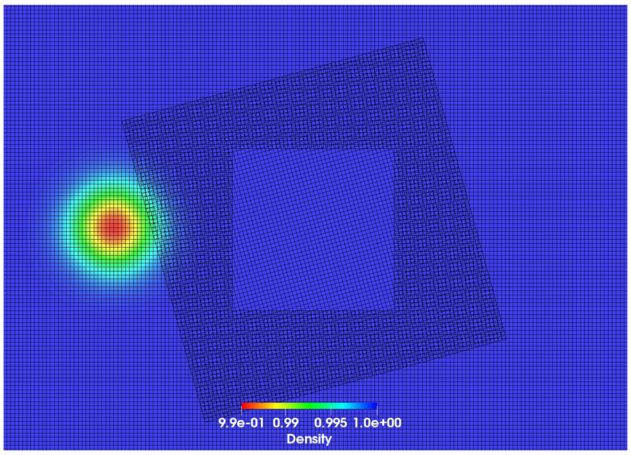

FIG. 14. The vortex passing through the overset rotating grid.

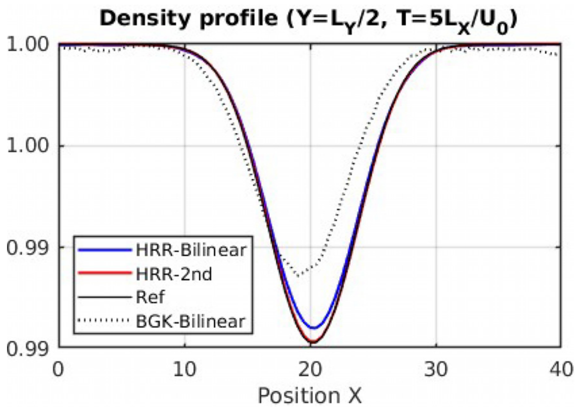

FIG. 15. Density profiles of the vortexes after 5 FTT. The vortex center is located at $L_x/5$.

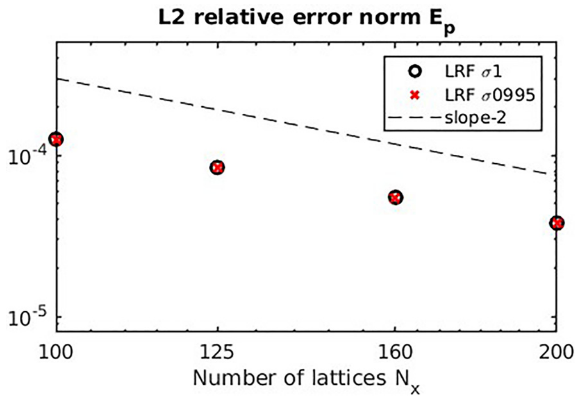

FIG. 16. L2 relative pressure error norms of the overset LRF simulations at different mesh resolutions. slope-2 legend denotes the slope of the second order accuracy.

$$E_p = \sqrt{\frac{\sum (p - p_{ref})^2}{\sum p_{ref}^2}}, \tag{37}$$

where the reference simulation is the HRR simulation without the overset grid. The number of lattices in the length of the domain is $N_x = 100, 125, 160, 200$ and the corresponding resolutions of lattices in the radius of the vortex are $N_{vortex} = 5, 6.25, 8, 10$. The errors are measured after three flow-through-times (FTT). The mesh convergence test is conducted for the overset method with the bilinear interpolation and the HRR models with different $\sigma = 1$ and $\sigma = 0.995$ are considered. It shows that the algorithm gives the second order accuracy at different mesh resolutions.

Acoustic properties of the vortex are then analyzed. Given the fact that the overset method with the bilinear interpolation would be more vulnerable to the spurious noise than the method with the second order interpolation, here the spurious noise is studied only with the bilinear interpolation. Pressure fluctuation $[p'(x,t) = \frac{\partial p}{\partial t}]$ is selected as a parameter to quantify the noise level.[51–53] Spurious noise generated from the overset LRF algorithm is evaluated by analyzing the pressure fluctuation p' between the overset LRF and reference computations ($|p' - p'_{ref}|$). From this parameter, the absolute spurious noise level can be identified, though it may not be sufficient to map detailed dissipation and dispersion properties of noise wave. Figure 17 plots the spurious noise when the center of the vortex is located at $(x, y) = (2L_x/5, L_y/2)$ which is the left edge of the square shaped fixed grid boundary in the middle of the computational domain. In the case of $\sigma = 1.0$ (Fig. 17, left), the spurious noise is emitted near the square boundary and then propagates through the field. However, introducing $\sigma = 0.995$ suppresses the level of the spurious noise (Fig. 17, right). It clearly shows that the spurious noise generated near the border is killed in the case of $\sigma = 0.995$. This effect is quantified by analyzing the power spectral density (Fig. 18). The power spectral density is calculated about the pressure fluctuation p' at the location $(x, y) = (4L_x/5, L_y/2)$ which is the coordinate at downstream of the

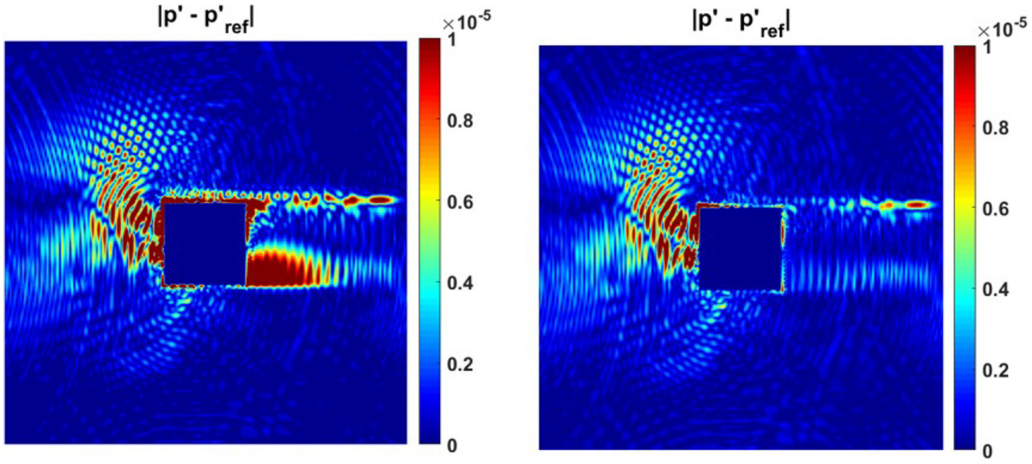

FIG. 17. Instantaneous spurious noise fields made by the overset LRF algorithm of the HRR model with different σ: $\sigma = 1.0$ (left) and $\sigma = 0.995$ (right). The error fields of the pressure fluctuations $p' = \frac{\partial p}{\partial t}$ after 1 FTT.

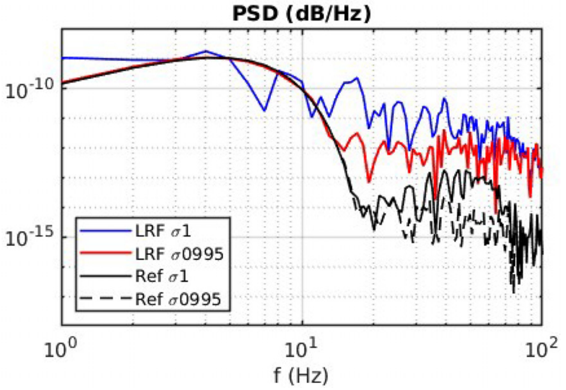

FIG. 18. Power spectral density of the pressure fluctuations $p' = \frac{\partial p}{\partial t}$ measured during 1 FTT. The reference simulations in the single fixed grid with $\sigma = 1.0$ and $\sigma = 0.995$ (solid black and dashed black). The overset LRF with $\sigma = 1.0$ (blue). The overset LRF with $\sigma = 0.995$ (red).

overset rotating mesh. The pressure fluctuation is measured during the time span of 1 FTT ($1\frac{L_x}{U_0}$). It shows that the $\sigma = 1.0$ case gives the spurious noise at various frequency levels. Particularly, the discrepancy in the power spectral density (PSD) between blue and black lines in Fig. 18 corresponds to the spurious noise. However, the level of spurious noise is reduced by introducing $\sigma = 0.995$ (a red line in Fig. 18). This effect of σ in suppressing the spurious noise corresponds to the observation which was studied in the context of the mesh refinement.[7]

C. Taylor–Couette flow

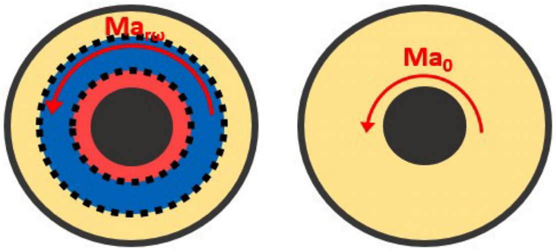

FIG. 19. Schematic views of the Taylor–Couette flow. Left: the overset LRF domain which comprises the fixed part of the overset grid (yellow and blue), the moving part of the overset grid (red and blue), and the overlapped part (blue). Right: the reference simulation in the single fixed grid.

The 2D Taylor–Couette flow is simulated using the overset LRF method. The HRR model with $\sigma = 1.0$ is used to run the both overset LRF and reference simulations. The inner rotating cylinder drives the flow while the outer cylinder is stationary. The local velocity at the wall of inner rotating cylinder is the Mach $Ma_0 = \frac{\omega R_i}{c_s} = 0.1$. The Reynolds number is $Re = \frac{\omega R_i(R_o - R_i)}{\nu} = 72$ and the corresponding dimensionless relaxation time is $\tau = \frac{1}{c_s^2}\frac{\nu}{\Delta t} + \frac{1}{2} = 0.62$. The radius of the outer stationary cylinder R_o is twice the inner rotating cylinder R_i, and therefore the aspect ratio is $\eta = \frac{R_i}{R_o} = 0.5$. The overset meshes are composed of the inner rotating mesh and the outer fixed mesh. The inner rotating mesh is attached to the rotating circular cylinder, where the wall boundary conditions are the no-slip velocity boundary condition ($u_\theta = 0$, $\frac{\partial u_r}{\partial n} = 0$) and the Neumann condition for density ($\frac{\partial \rho}{\partial n} = 0$). Although it employs the no-slip velocity condition, it could actualize flow characteristics of the rotating solid because the whole inner mesh is rotating as it is being attached to the inner cylinder. The radius of the overset rotating grid is $R_{mg} = 1.6R_i$, and hence the mesh velocity at the outer radius of the overset rotating grid is $Ma_{r\omega} = \frac{R_{mg}\omega}{c_s} = 0.16$. The outer mesh is affixed to the outer stationary curved wall having the no-slip velocity boundary condition ($u_\theta = 0$, $\frac{\partial u_r}{\partial n} = 0$) and the Neumann boundary condition for density ($\frac{\partial \rho}{\partial n} = 0$). As a reference, the computational domain with the single fixed mesh is chosen by imposing the slip-wall velocity Ma_0 on the curved cylinder wall. Schematic diagrams of the overset LRF and reference domains are given in Fig. 19. The initial flow condition of the azimuthal velocity $u_{\theta,t=0}$ is defined as the analytical Taylor–Couette solution ($u_{\theta,t=0} = Ar + \frac{B}{r}, A = -\omega\frac{\eta^2}{1-\eta^2}, B = \omega R_i^2 \frac{1}{1-\eta^2}$, r: the radius from the rotation center), while the initial radial velocity and density are set as uniform ($u_{r,t=0} = 0, \rho_{t=0} = \rho_0$). The iteration is stopped when the convergence criteria is reached $\left[\frac{\sum ||u(x,t+1) - u(x,t)||}{\sum ||u(x,t)||} < 10^{-7}\right]$.

Figure 20 compares the velocity profile of the overset LRF computation with the reference. The velocity is normalized by the local velocity at the wall. The red line refers the velocity profile at the inner rotating mesh and the blue line is the velocity at the outer fixed mesh. The green line is the velocity profile of the reference computation which is from the single fixed mesh. The number of lattices in the diameter of the inner solid cylinder is $N_d = 125$. The inner boundary of the fixed part of the overset LRF grids is located at $\frac{R}{Ro} = 0.7$ (Fig. 20), where the interpolation from the moving to fixed grid occurs. Meanwhile, the outer boundary of the rotating part of the overset LRF grids is placed at $\frac{R}{Ro} = 0.8$ (Fig. 20), where the rotating grid receives the information from the fixed grid through the interpolation. The result shows that the both profiles are well matched. Figure 21 describes the normalized pressure profiles of the overset LRF and reference computations. The pressure profiles are normalized by the

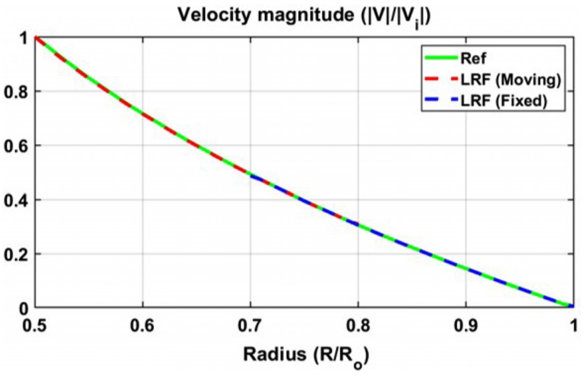

FIG. 20. Velocity magnitude profiles of the Taylor–Couette flow. The reference simulation in the single fixed grid (green). The inner rotating part of the overset LRF grids (red). The outer fixed part of the overset LRF grids (blue). V_i is the velocity at the inner rotating wall. R_o is the radius of the outer stationary wall.

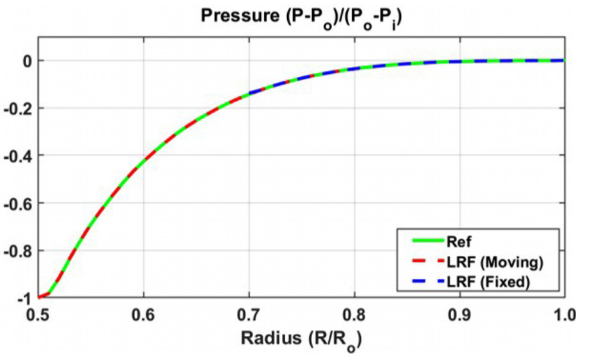

FIG. 21. Pressure profiles of the Taylor-Couette flow. The reference simulation in the single fixed grid (green). The inner rotating part of the overset LRF grids (red). The outer fixed part of the overset LRF grids (blue). P_i is the pressure at the inner rotating wall. P_o is the pressure at the outer stationary wall. R_o is the radius of the outer stationary wall.

pressure at the inner rotating wall (P_i) and the outer boundary wall (P_o), and both results are well matched.

A mesh convergence test is conducted for the Taylor–Couette flow computation of the overset LRF algorithm. The L2 relative errors of velocity fields are computed between the overset LRF results and the reference computations at different mesh resolutions [Eq. (38)]. N_d indicates the number of lattices in the diameter of the inner rotating cylinder. Figure 22 shows that the overset LRF has second order accuracy in the mesh convergence test. The overset LRF method is able to achieve this second order accuracy because all its related components have the second order accuracy. For example, the LRF method uses the extrapolation based no-slip wall boundary condition which has the second order accuracy.[31] Also, the accuracy of the forcing term inside the rotating region is reported as having the second order accuracy.[22,24,27] That is why the overset LRF algorithm is able to achieve the robust second order accuracy,

$$E_u = \sqrt{\frac{\sum (u - u_{ref})^2}{\sum u_{ref}^2}}. \tag{38}$$

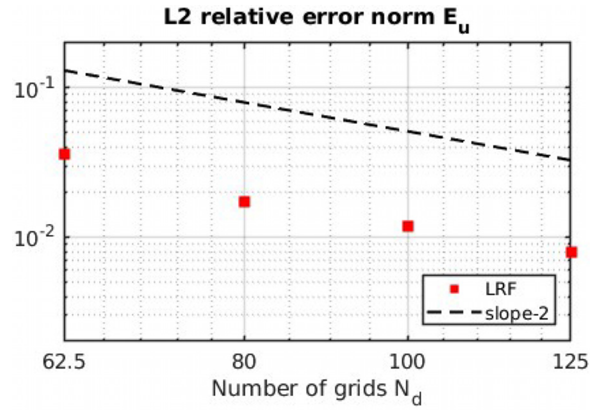

FIG. 22. L2 relative velocity error norms of the overset LRF simulations at different mesh resolutions. N_d is the number of lattices in the diameter of inner rotating cylinder driving the Taylor-Couette flow.

D. Rotating circular cylinder in uniform flow

A rotating circular cylinder in a uniform stream is chosen to further assess the overset LRF algorithm. The Mach number of inlet flow is $Ma_0 = 0.03$, while varying the rotation ratio a of the circular cylinder from 0.5 to 2.0. The rotation ratio a is defined as the ratio between the local velocity at the rotating cylinder wall and the free stream velocity ($a = \frac{\omega R}{U_0}$). The Reynolds number is $Re = 200$ where the flow becomes unsteady ($Re = \frac{2U_0 R}{\nu}$). The height and length of the computational domain L are set equal to $200R$ which is large enough to avoid reflected disturbance from the inlet, outlet, and surrounding walls. The HRR model with $\sigma = 1.0$ is employed within the D3Q19 lattice, but the computational domain is quasi-2D by setting the periodic boundaries in the depth direction.

The mesh refinement is applied to save the number of lattices while keeping the fine resolution in the vicinity of the solid cylinder. In the test case with $Re = 200$, the size of the finest lattice near the cylinder is $\Delta X = \frac{R}{20}$, which means that the number of lattices on the radius of cylinder is 20. In the outermost region, the resolution is the coarsest having the size of lattice as $\Delta X = \frac{R}{2.5}$. The finest region in the core of multi-level grids has the length $12R$. Figure 23 shows the mesh structure which is composed of four different mesh levels, where the mesh resolution is increased two times at each transition interface. The inlet boundary condition is Dirichlet velocity and the Neumann for density. The outlet boundary condition is Dirichlet density and the Neumann boundary condition for velocity. Top and bottom boundaries have the slip boundary condition, whereas velocity and density are defined using the Neumann boundary condition and shear stress parallel to the wall is null. The radius of overset rotating mesh is large enough to avoid disturbance between the boundary of rotating mesh and the solid circular cylinder ($R_{mesh} = 3R$), which makes the local velocity at the boundary of overset rotating mesh to be three times of the local velocity at the rotating cylinder wall. For example, when the rotation ratio a is 2.0, the local velocity at the rotating cylinder wall is around 0.06 (aMa_0) and the local velocity at the boundary of the rotating mesh becomes around 0.18 ($3aMa_0$). If the rotation ratio is increased more, then the accuracy of the simulation will be affected due to the higher local velocity at the outer rotating mesh boundary.

Lift and drag coefficients are compared with the reference cases which are computed from the direct numerical simulation of Navier–Stokes computation.[54] The aerodynamic coefficients are computed by applying the far-field integral method,[55,56] which are

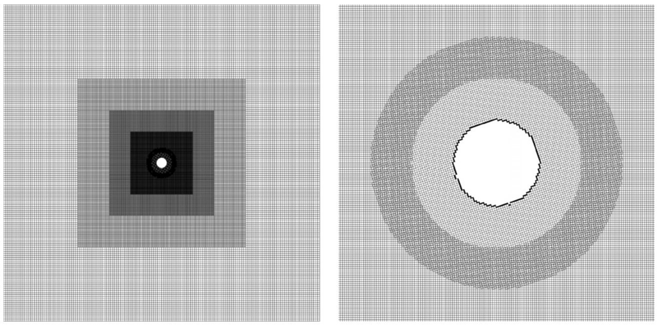

FIG. 23. The mesh refinement structure in global view (left). The mesh structure near the rotating solid cylinder in close view (right).

averaged over 1 FTT ($1\frac{L}{U_0}$). Figure 24 shows the averaged lift and drag coefficients and the Strouhal number. The averaged lift and drag coefficients are well matched with the references (Fig. 24, top and middle). All over the different rotation ratios a from 0.5 to 2.0, errors of averaged lift and drag coefficients are less than 1%, but with the higher rotation ratio near $a = 3.0$, the error becomes increased due to the elevated local Mach number inside the rotating region. Also, the Magnus effect is well captured, which means that the flow unsteadiness is faded away as the rotation ratio a reaches 2.0 (Fig. 24, bottom). The Strouhal number shows that the flow becomes steady when the rotation ratio is 2.0. The Strouhal number references are not provided for $a = 2.5 - 3.0$ due to their availability in the reference. Instantaneous flow fields show that the re-circulation zone behind the cylinder is well identified compared to the Navier–Stokes reference (Fig. 25, left) and the Karman vortex structure is well observed (Fig. 25, right),

$$C_D = \frac{F_x}{\rho R U_0^2}, \quad C_L = \frac{F_y}{\rho R U_0^2}, \quad St = \frac{2fR}{U_0}. \tag{39}$$

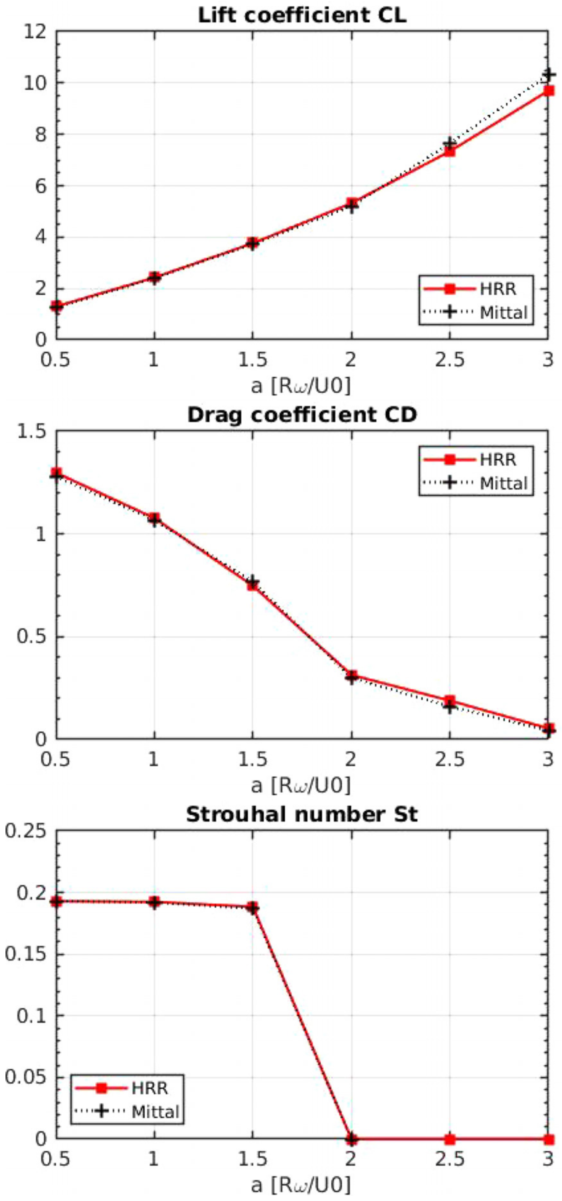

FIG. 24. Aerodynamic coefficients at different rotation ratios in the Reynolds number $Re = 200$. The averaged lift coefficients (top), the averaged drag coefficients (middle), and the Strouhal number (bottom).

E. Large-eddy simulation of flow over a 3D rotating cylinder

The turbulent flow past a 3D rotating circular cylinder in a uniform flow is simulated by the overset LRF algorithm. The Mach number of inlet flow is $Ma_0 = 0.0735$, while the rotation ratio a of the circular cylinder is $a = 1.0$ ($a = \frac{\omega R}{U_0}$). The Reynolds number is $Re = \frac{2U_0R}{\nu} = 5 \times 10^3$. The height of channel is set as $H = 80R$ and the distance from the inlet is $20R$ and from the outlet is $80R$. The depth of the channel is $Z = 6.4R$. The HRR model with $\sigma = 1.0$ is employed within the D3Q19 lattice, by using the gradient based second order interpolation scheme. The large eddy simulation is performed using the shear-improved Smagorinsky model to model the subgrid scale turbulence.[57] The Dirichlet type no-slip wall boundary condition is imposed on the rotating cylinder. The first cell height at the top of the cylinder is located near $r^+ = 1.61$.

The mesh refinement is applied to spare the number of lattices while keeping a fine resolution near the 3D rotating cylinder.[58] The size of the finest lattice near the cylinder is $\Delta X = \frac{R}{50}$, which means that there are 50 lattices in the radius of cylinder. The coarsest lattice resolution is $\Delta X = \frac{R}{1.5625}$. Figure 26 shows the mesh structure which is composed of five different mesh levels. The inlet boundary condition is Dirichlet velocity and the Neumann for density.[32] The outlet boundary condition is Dirichlet density and the Neumann boundary condition for velocity.[32] Top and bottom walls have frictionless slip wall boundary conditions.[32] Each boundary is equipped with a sponge zone to prevent spurious reflections.[32] The radius of overset rotating mesh is $R_{mesh} = 3R$, which gives the local velocity at the boundary of the rotating mesh to be around $Ma_{mesh} = 0.22$.

The aerodynamic coefficients are compared with the reference cases which are computed from the large eddy simulation (LES) of Navier–Stokes based computation.[59] The coefficients are evaluated from the far-field integral method,[55,56] which is averaged over 80 non-dimensional time span ($= \frac{tU_0}{2R}$) after the simulation has reached a statistically steady state. Table II displays the averaged aerodynamic coefficients computed using the HRR collision model which are close to the references within 5% of error. Also, 3D vortex structure is observed by using the isosurface Q-criterion, which describes a vortex shedding over the 3D cylinder (Fig. 27).

VI. CONCLUSION

The overset LRF grid with HRR collision model has been assessed for simulating rotating geometries. The discrete forcing scheme is well established to consider the fictitious forces inside the overset rotating region. Also, the interpolation between the rotating and fixed grids is conducted through the macroscopic quantities. The HRR model

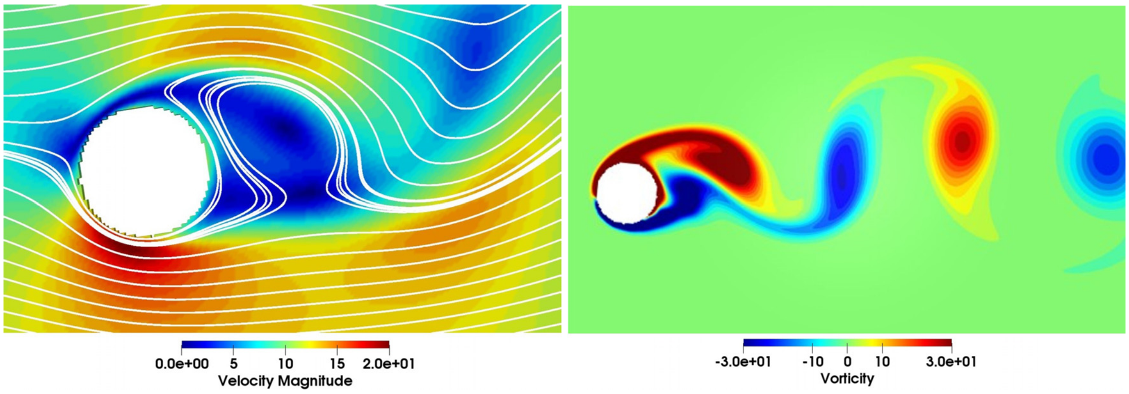

FIG. 25. Velocity streamlines (left) and vorticity field (right) in $Re = 200$, $a = 1.0$.

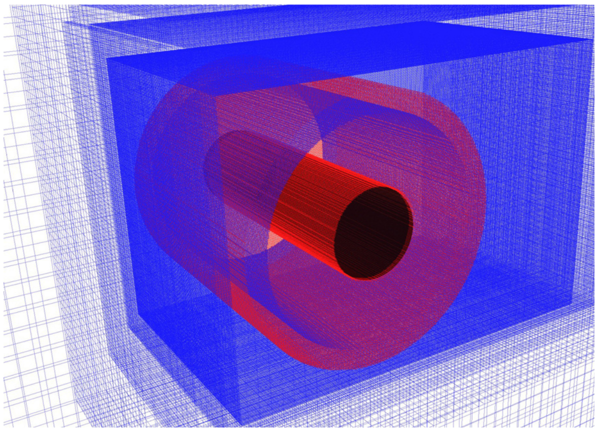

FIG. 26. 3D overset mesh structure: fixed mesh (blue), rotating mesh (red), and the rotating cylinder (black).

TABLE II. Aerodynamic coefficients ($Re = 5 \times 10^3$, $a = 1.0$).

	Mobini and Niazi[59]	HRR
C_L	1.880	1.875
C_D	0.810	0.819

successfully proves its capability to stabilize the overset LRF algorithm as overcoming its numerical defects.

The HRR model is observed to contribute to enhancing accuracy of the discrete forcing scheme by suppressing the spurious error in the non-equilibrium tensor, as outperforming the BGK model (see Sec. IV A). Also, it is demonstrated that the stability of the overset algorithm is improved by injecting artificial viscosity, by tuning the parameter σ in the HRR model, but it can also overdamp the simulation by reducing the order of accuracy (see Sec. IV B). Then, different interpolation methods have been considered, showing that the higher order Hermite interpolation can reduce the spurious errors efficiently (see Sec. IV C).

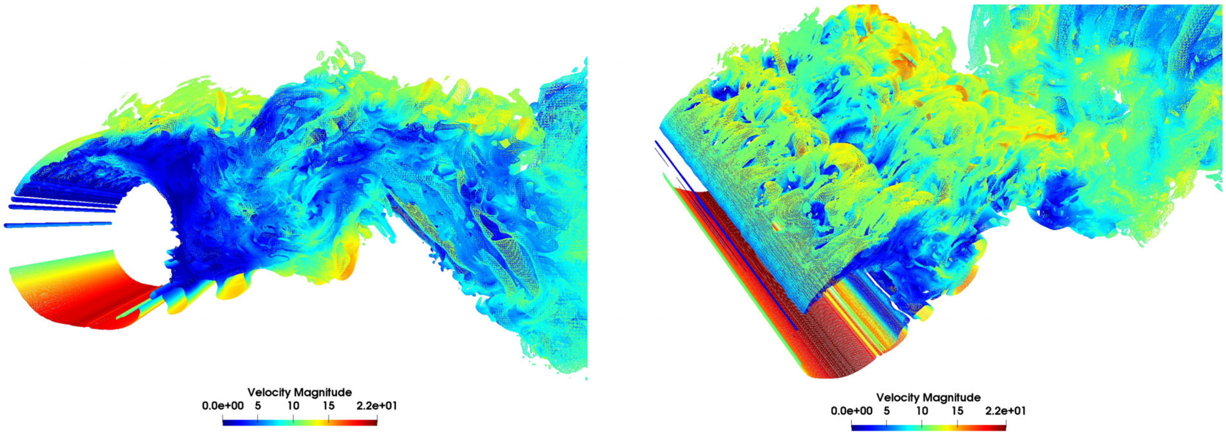

FIG. 27. Isosurface Q-criterion colored by velocity in side-view (left) and top-view (right).

The robustness of the overset-HRR method is assessed with the empty rotating sub-domain in the high Reynolds and moderate Mach number flows. It shows that the spurious velocity error of the overset algorithm is lower than the BGK at different forcing schemes, without diverging according to time (see Sec. V A). Also, the second order accuracy at different mesh resolutions is achieved in the vortex advection test case. It shows that the second order interpolation is more effective to keep the vortex structure than the bilinear interpolation. And, the way how its spurious acoustic noise is damped by injecting the artificial viscosity is presented (see Sec. V B).

Furthermore, the overset method is tested with the rotating solid body in the mid-to-high Reynolds and Mach number flows. It achieves the second order accuracy at different mesh resolutions in the Taylor–Couette flow test case (see Sec. V C). Also, in $Re = 200$, the errors of aerodynamic coefficients are less than 1% compared to the Navier–Stokes based references for the test case with a 2D rotating circular cylinder in uniform channel flow (see Sec. V D). Finally, a 3D rotating circular cylinder is tested in high Re flow by using the large eddy simulation approach, which is validated from the reasonable aerodynamic coefficients compared to the reference (see Sec. V E).

This research confirms the performance of the overset LRF method in the framework of the hybrid recursive regularized collision model. To the best of the authors' knowledge, this is the first research which tests the regularization based collision model with the overset method. The scheme is validated by demonstrating its second order accuracy at different test cases and its aerodynamic profiles are validated from the references. In close-term perspective, the authors expect that this work could deal with industrial applications such as higher Reynolds number flows with turbulence models, 3D flows, and compressible flows.

ACKNOWLEDGMENTS

The author H. Yoo thanks Dr. Ricot (Renault) and Dr. Sengissen (Airbus) for fruitful discussions about the overset method and moving geometries. This work was supported by ANR Industrial Chair ALBUMS (Grant No. ANR-18-CHIN-0003–01). The ProLB solver was used to perform the work.

DATA AVAILABILITY

The data that support the findings of this study are available from the corresponding author upon reasonable request.

REFERENCES

[1] J. Latt and B. Chopard, "Lattice Boltzmann method with regularized pre-collision distribution functions," Math Comput. Simul. **72**, 165–168 (2006).

[2] O. Malaspinas, "Increasing stability and accuracy of the Lattice Boltzmann scheme: Recursivity and regularization," arXiv:1505.06900 [physics.flu-dyn] (2015).

[3] C. Coreixas, G. Wissocq, G. Puigt, J.-F. Boussuge, and P. Sagaut, "Recursive regularization step for high-order lattice Boltzmann methods," Phys. Rev. E **96**, 033306 (2017).

[4] J. Jacob, O. Malaspinas, and P. Sagaut, "A new hybrid recursive regularised Bhatnagar–Gross–Krook collision model for Lattice Boltzmann method-based large eddy simulation," J. Turbul. **19**, 1051–1076 (2018).

[5] Y. Feng, P. Boivin, J. Jacob, and P. Sagaut, "Hybrid recursive regularized thermal lattice Boltzmann model for high subsonic compressible flows," J. Comput. Phys. **394**, 82–99 (2019).

[6] G. Farag, S. Zhao, T. Coratger, P. Boivin, G. Chiavassa, and P. Sagaut, "A pressure-based regularized lattice-Boltzmann method for the simulation of compressible flows," Phys. Fluids **32**, 066106 (2020).

[7] T. Astoul, G. Wissocq, J.-F. Boussuge, A. Sengissen, and P. Sagaut, "Analysis and reduction of spurious noise generated at grid refinement interfaces with the lattice Boltzmann method," J. Comput. Phys. **418**, 109645 (2020).

[8] F. Renard, G. Wissocq, J. Boussuge, and P. Sagaut, "A linear stability analysis of compressible hybrid lattice Boltzmann methods," arXiv:2006.08477 (2020).

[9] G. Wissocq, C. Coreixas, and J.-F. Boussuge, "Linear stability and isotropy properties of athermal regularized lattice Boltzmann methods," Phys. Rev. E **102**, 053305 (2020).

[10] Z.-G. Feng and E. E. Michaelides, "The immersed boundary-lattice Boltzmann method for solving fluid–particles interaction problems," J. Comput. Phys. **195**, 602–628 (2004).

[11] L. Zhu, G. He, S. Wang, L. Miller, X. Zhang, Q. You, and S. Fang, "An immersed boundary method based on the lattice Boltzmann approach in three dimensions, with application," Comput. Math. Appl. **61**, 3506–3518 (2011).

[12] J. Favier, A. Revell, and A. Pinelli, "A Lattice Boltzmann–Immersed Boundary method to simulate the fluid interaction with moving and slender flexible objects," J. Comput. Phys. **261**, 145–161 (2014).

[13] L. Xu, F.-B. Tian, J. Young, and J. C. Lai, "A novel geometry-adaptive Cartesian grid based immersed boundary–lattice Boltzmann method for fluid–structure interactions at moderate and high Reynolds numbers," J. Comput. Phys. **375**, 22–56 (2018).

[14] M. Specklin, P. Dubois, A. Albadawi, and Y. Delauré, "A full immersed boundary solution coupled to a lattice–Boltzmann solver for multiple fluid–structure interactions in turbulent rotating flows," J. Fluids Struct. **90**, 205–229 (2019).

[15] S. Nishimura, K. Hayashi, S. Nakaye, M. Yoshimoto, K. Suga, and T. Inamuro, "Implicit large-eddy simulation of rotating and non-rotating machinery with cumulant lattice Boltzmann method aiming for industrial applications," in AIAA Aviation 2019 Forum (2019).

[16] R. Zhang, C. Sun, Y. Li, R. Satti, R. Shock, J. Hoch, and H. Chen, "Lattice Boltzmann approach for local reference frames," Commun. Comput. Phys. **9**, 1193–1205 (2011).

[17] Y. Li, "An improved volumetric LBM boundary approach and its extension for sliding mesh simulation," Ph.D. thesis (Iowa State University, 2011).

[18] F. Perot, M.-S. Kim, and M. Meskine, "NREL wind turbine aerodynamics validation and noise predictions using a lattice Boltzmann method," *18th AIAA/CEAS Aeroacoustics Conference (33rd AIAA Aeroacoustics Conference)* (2012).

[19] E. K. Far, M. Geier, and M. Krafczyk, "Simulation of rotating objects in fluids with the cumulant lattice Boltzmann model on sliding meshes," Comput. Math. Appl. **79**, 3–16 (2020).

[20] P. Lallemand and L.-S. Luo, "Lattice Boltzmann equation with Overset method for moving objects in two-dimensional flows," J. Comput. Phys. **407**, 109223 (2020).

[21] P. Bhatnagar, E. Gross, and M. Krook, "A model for collision processes in gases. I. Small amplitude processes in charged and neutral one-component systems," Phys. Rev. **94**(3), 511–525 (1954).

[22] T. Krüger, H. Kusumaatmaja, A. Kuzmin, O. Shardt, G. Silva, and E. M. Viggen, *The Lattice Boltzmann Method—Principles and Practice* (Springer International Publishing, 2016), pp. 251–282.

[23] S. Chapman and T. G. Cowling, *The Mathematical Theory of Non-Uniform Gases* (Cambridge University Press, 1953).

[24] Z. Guo, C. Zheng, and B. Shi, "Discrete lattice effects on the forcing term in the lattice Boltzmann method," Phys. Rev. E **65**, 046308 (2002).

[25] P. J. Dellar, "An interpretation and derivation of the lattice Boltzmann method using Strang splitting," Comput. Math. Appl. **65**, 129–141 (2013).

[26] R. Salmon, "Lattice Boltzmann solutions of the three-dimensional planetary geostrophic equations," J. Mar. Res. **57**, 847–884 (1999).

[27] G. Silva and V. Semiao, "First- and second-order forcing expansions in a lattice Boltzmann method reproducing isothermal hydrodynamics in artificial compressibility form," J. Fluid Mech. **698**, 282–303 (2012).

[28] W. H. Press, S. A. Teukolsky, W. T. Vetterling, and, and B. P. Flannery, *Numerical Recipes in C: The Art of Scientific Computing*, 2nd ed. (Cambridge University Press, New York, 1992), pp. 123–128.

[29] P. M. Hummel, "The accuracy of linear interpolation," Am. Math. Mon. **53**, 364–366 (1946).

[30] J. Tölke and M. Krafczyk, "Second order interpolation of the flow field in the lattice boltzmann method," Comput. Math. Appl. **58**, 898–902 (2009).

[31] O. Malaspinas, B. Chopard, and J. Latt, "General regularized boundary condition for multi-speed lattice Boltzmann models," Comput. Fluids **49**, 29–35 (2011).

[32] Y. Feng, S. Guo, J. Jacob, and P. Sagaut, "Solid wall and open boundary conditions in hybrid recursive regularized lattice Boltzmann method for compressible flows," Phys. Fluids **31**, 126103 (2019).

[33] A. J. C. Ladd, "Numerical simulations of particulate suspensions via a discretized Boltzmann equation. Part 1. Theoretical foundation," J. Fluid Mech. **271**, 285–309 (1994).

[34] I. Ginzburg and D. d'Humières, "Multireflection boundary conditions for lattice Boltzmann models," Phys. Rev. E **68**, 066614 (2003).

[35] M. Meldi, E. Vergnault, and P. Sagaut, "An arbitrary Lagrangian–Eulerian approach for the simulation of immersed moving solids with lattice Boltzmann method," J. Comput. Phys. **235**, 182–198 (2013).

[36] G. Silva, "Discrete effects on the forcing term for the lattice Boltzmann modeling of steady hydrodynamics," Comput. Fluids **203**, 104537 (2020).

[37] D. Lycett-Brown and K. H. Luo, "Improved forcing scheme in pseudopotential lattice Boltzmann methods for multiphase flow at arbitrarily high density ratios," Phys. Rev. E **91**, 023305 (2015).

[38] M. B. Reider and J. D. Sterling, "Accuracy of discrete-velocity BGK models for the simulation of the incompressible Navier-Stokes equations," Comput. Fluids **24**, 459–467 (1995).

[39] P. A. Skordos, "Initial and boundary conditions for the lattice Boltzmann method," Phys. Rev E **48**, 4823–4842 (1993).

[40] X. He and L.-S. Luo, "Lattice Boltzmann model for the incompressible Navier–Stokes equation," J. Stat. Phys. **88**, 927–944 (1997).

[41] D. J. Holdych, D. R. Noble, J. G. Georgiadis, and R. O. Buckius, "Truncation error analysis of lattice Boltzmann methods," J. Comput. Phys. **193**, 595–619 (2004).

[42] S. Ubertini, P. Asinari, and S. Succi, "Three ways to lattice Boltzmann: A unified time-marching picture," Phys. Rev. E **81**, 16311 (2010).

[43] J. M. Buick and C. A. Greated, "Gravity in a lattice Boltzmann model," Phys. Rev. E **61**, 5307–5320 (2000).

[44] T. Krüger, F. Varnik, and D. Raabe, "Shear stress in lattice Boltzmann simulations," Phys. Rev. E **79**, 046704 (2009).

[45] S. Hou, Q. Zou, S. Chen, G. Doolen, and A. C. Cogley, "Simulation of cavity flow by the lattice Boltzmann method," J. Comput. Phys. **118**, 329–347 (1995).

[46] D. Ricot, S. Marié, P. Sagaut, and C. Bailly, "Lattice Boltzmann method with selective viscosity filter," J. Comput. Phys. **228**, 4478–4490 (2009).

[47] P. J. Dellar, "Bulk and shear viscosities in lattice Boltzmann equations," Phys. Rev. E **64**, 031203 (2001).

[48] X. He, "Error analysis for the interpolation-supplemented lattice-Boltzmann equation scheme," Int. J. Mod. Phys. C **8**, 737–745 (1997).

[49] X. He, X. Shan, and G. Doolen, "Discrete Boltzmann equation model for nonideal gases," Phys. Rev. E **57**, R13 (1998).

[50] G. Wissocq and J.-F. Boussuge, "Consistent vortex initialization for the athermal lattice Boltzmann method," Phys. Rev. E **101**, 043306 (2020), https://doi.org/10.1103/PhysRevE.101.043306

[51] G. Wang, F. Duchaine, D. Papadogiannis, I. Duran, S. Moreau, and L. Y. Gicquel, "An overset grid method for large eddy simulation of turbomachinery stages," J. Comput. Phys. **274**, 333–355 (2014).

[52] V. B. Ananthan, P. Bernicke, and R. A. D. Akkermans, "Aeroacoustic analysis of a circulation-controlled high-lift flap by zonal overset large-eddy simulation," AIAA J. **58**, 5294–5305 (2020).

[53] A. H. Dawi and R. A. Akkermans, "Spurious noise in direct noise computation with a finite volume method for automotive applications," Int. J. Heat Fluid Flow **72**, 243–256 (2018).

[54] S. Mittal and B. Kumar, "Flow past a rotating cylinder," J. Fluid Mech. **476**, 303–334 (2003).

[55] H. Toubin and D. Bailly, "Development and application of a new unsteady far-field drag decomposition method," AIAA J. **53**, 3414–3429 (2015).

[56] M. Gariepy, J.-Y. Trepanier, and B. Malouin, "Generalization of the far-field drag decomposition method to unsteady flows," AIAA J. **51**, 1309–1319 (2013).

[57] H. Touil, D. Ricot, and E. Lévêque, "Direct and large-eddy simulation of turbulent flows on composite multi-resolution grids by the lattice Boltzmann method," J. Comput. Phys. **256**, 220–233 (2014).

[58] Y. Feng, S. Guo, J. Jacob, and P. Sagaut, "Grid refinement in the three-dimensional hybrid recursive regularized lattice Boltzmann method for compressible aerodynamics," Phys. Rev. E **101**, 063302 (2020).

[59] K. Mobini and M. Niazi, "Large eddy simulation of the flow across a rotating circular cylinder," Int. J. Fluid Mech. Res. **41**, 1–15 (2014).